IAEA
International Atomic Energy Agency

Hands-on Training Courses Using Research Reactors and Accelerators

VIENNA, 2014

TRAINING COURSE SERIES

4. ACCELERATOR APPLICATIONS EXPERIMENTS

4.1. STOPPING POWER OF LIGHT IONS IN SOLID MATERIALS

4.1.1. Theoretical background

Energetic ions lose energy when passing through materials due to Coulomb interactions with atomic electrons and nuclei. At MeV ion energies, the dominant energy loss mechanism is through interactions with electrons (electronic stopping power). At keV and lower energies, the transfer of energy to the atomic nuclei becomes more important (nuclear stopping power). The sum of these two energy loss processes is the total stopping power *S(E)*, which is defined as the rate of energy lost per unit distance:

$$S(E) = \frac{dE}{dx} \tag{57}$$

In the MeV energy region, nuclear stopping only contributes a few percent to total stopping power. In this region, the electronic stopping power *S(E)* is described by the Bethe-Bloch equation [12, 13]:

$$S(E) = 4\pi r_0^2 mc^2 \frac{Z_1^2}{\beta^2}\frac{Z_2}{M_2} N_A \ln\left(\frac{2mc^2}{I}\beta^2 - U\right) \tag{58}$$

$$\beta = \frac{v_1}{c}$$

Where r_0 is the classical electron radius (2.8 fm), Z_1 and Z_2 are the projectile and target atomic number, M_2 the mass of the target atom, N_A Avogadro's number, I the mean ionisation potential of the target material, U a shell correction factor, and β the ratio of projectile speed to the speed of light.

In practice, a semi-empirical model of stopping powers is used SRIM [14], which uses best-fits on experimentally measured data. This freely-available and widely-used software is used to calculate stopping powers for different ion/material combinations. For this experiment, the stopping power of protons in aluminium is used, with the calculations of SRIM plotted in Figure 21.

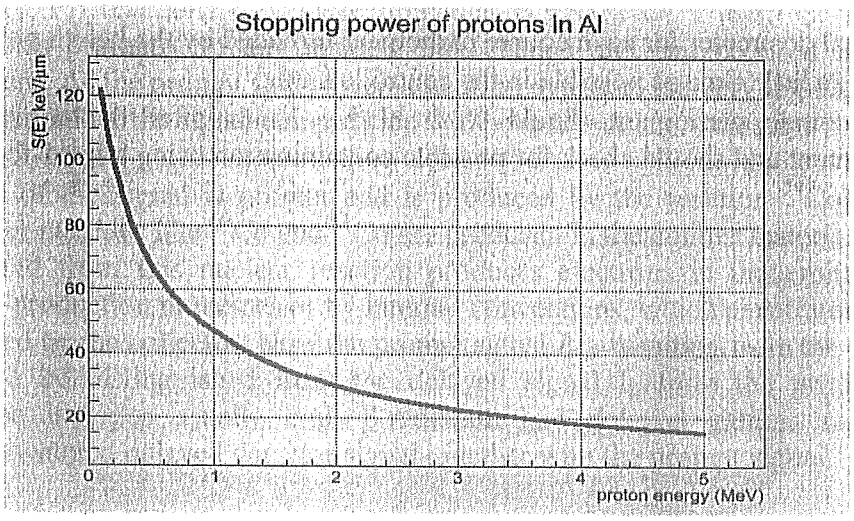

FIG. 21. Stopping power of protons in aluminium calculated by SRIM.

A commonly encountered experimental situation is shown in Figure 22. An ion beam of energy E_0 traverses a material of thickness Δx, exiting with an energy loss of ΔE.

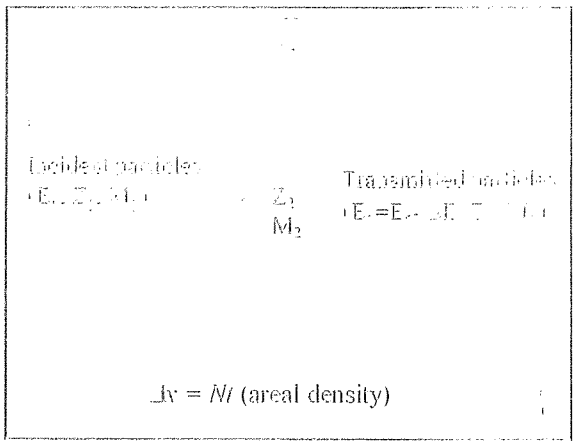

FIG. 22. Schematic diagram of the incident ion (Z_1, M_1) passing through a homogeneous material with thickness Δx composed of atoms with atomic number Z_2 and mass M_2.

The energy E_1 of the ion after passing through the thickness Δx is given by Eq. (59):

$$E_1 = E_0 - \Delta E = \int_0^x \frac{dE}{dx}\, dx \tag{59}$$

To find the material thickness Δx producing a given energy change ΔE, one must invert $\frac{dE}{dx}$ and integrate over energy:

$$\Delta x = \int_{E_1}^{E_0} \left(\frac{dE}{dx} \right)^{-1} dE \tag{60}$$

This integration can be done numerically or by slab analysis. For thin targets in which $\frac{dE}{dx}$ does not significantly change as the ion beam passes through the material, the stopping power can be taken as a constant and to be that value at the surface of the material. Eq. (60) thus becomes:

$$\Delta x = \frac{\Delta E}{\left(\frac{dE}{dx} \right)_{E=E_0}} = \frac{\Delta E}{S(E_0)} \tag{61}$$

3.1.1. Experimental procedure

The measurements must be carried out in a vacuum chamber. The chamber should be light-tight so the charged particle detector is sensitive to light reflected from or emitted by the experimental device in Figure 23. The foil specimen should be mounted on a thin, self-

These scattered protons are incident on a foil of unknown thickness. The transmitted protons are detected in the particle detector. The measured energy spectra are shown in Figure 24.

The energy loss of beam particles in the foil should be smaller than the energy resolution of the particle detector (~ 15 keV). The diameter of the incident beam on the target was 3 mm, and the proton beam current is kept below 10 nA during the measurement. Two options for the experimental setup are shown in Figure 23.

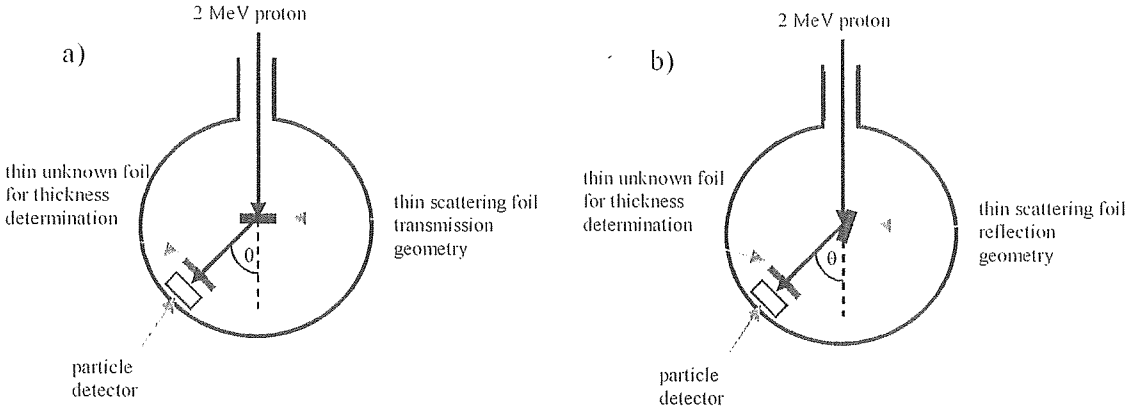

FIG. 23. Setup of the experiment for foil thickness determination: a) with a scattering foil in the transmission geometry, b) with a scattering foil in the reflection geometry.

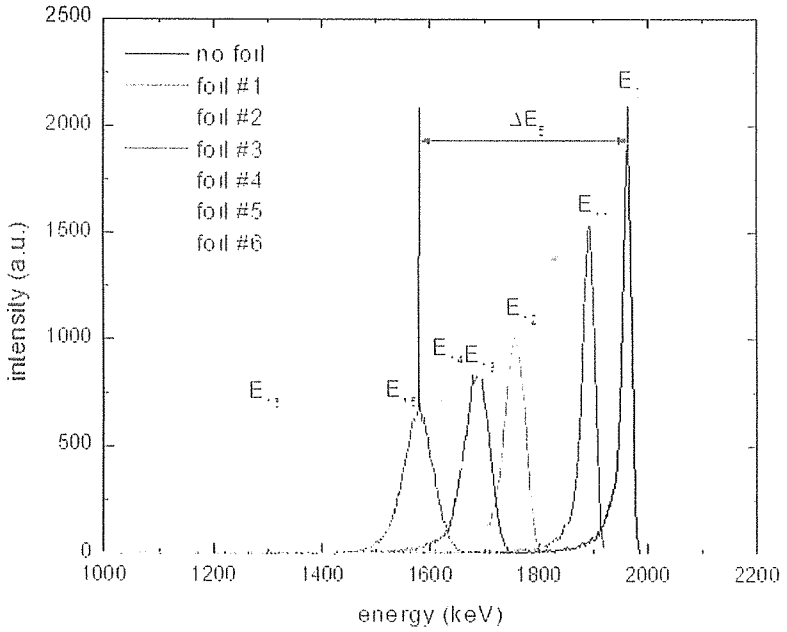

FIG. 24. Energy spectra of 2 MeV protons scattered from thin gold foil after passing through aluminium foils of different thicknesses and scattered with no foil in front of detector (black line).

The final energy of the ion after passing through the thin aluminium foil can be found from the peak position in the energy spectrum, as shown at Figure 24. First, the position and the width of the peak in the energy spectrum of 2 MeV protons scattered from the thin Au foil is measured using the particle detector. This defines the initial condition E_0. Next, foils of

different thicknesses are placed in front of the particle detector. The peak position and its width are determined for each foil. It is assumed that the energy calibration of the particle detector is well-known. If not, it should be done before measurement e.g. by measuring forward scattering spectra from the thin gold foil at a minimum of two different proton energies and constructing a linear calibration using the reaction kinematics.

Aluminium foils have been used for these measurements; however, more readily available thin foils of other materials (e.g. Mylar™ or Kapton™) can be used. The prerequisite condition is that the foils are thin enough so that 2 MeV protons can be transmitted through them into the detector. Different thicknesses can be obtained by adding together different combinations of the available thin foils. The areal density of the thin foils can be determined by precise weighing and measurement of the foil area. The foil density (g/cm^3) should be known to obtain a nominal physical thickness. These foil thicknesses will be compared with those determined from the energy loss experiment.

In this experiment, 6 aluminium foils of different thicknesses are measured, as shown in Figure 24. The thickness of foils #3 - #6 was determined by weighting, while the thicknesses of foils #1 and #2 were given by the foil supplier. All spectra were accumulated to the approximately same number of detected protons. The peak in the energy spectrum of 2 MeV protons forward scattered from the gold foil (black line) and detected by the particle detector is defined by the position of energy E_0. Subsequently, spectra are recorded with different aluminium foils placed in front of the particle detector. The energy E_{1n} when foil #n is placed in front of particle detector is denoted in Eq. (62):

$$E_{1n} = E_0 - \Delta E_n \tag{62}$$

Here ΔE_n is the energy loss of protons in the n^{th} foil as is shown on Figure 24.

The foil thicknesses determined from the stopping power measurements, together with the thicknesses that are given by foil suppliers or weighed, are given in Table 20. The average uncertainty is dominated by uncertainty in the stopping power (< 4% for H in Al) and uncertainty in the centroid position of the peak to be < 7%.

TABLE 20. COMPARISON OF THICKNESSES OF DIFFERENT Al FOILS FROM ENERGY LOSS MEASUREMENTS IN COMPARISON WITH FOIL THICKNESSES GIVEN BY FOIL PRODUCERS OR FROM WEIGHT MEASUREMENTS (1 μm Al = 6024 × 10^{15} at/cm^2)

Foil #	ΔE (keV)	t_{Al} (10^{15} at/cm^2)	t_{Al} (from Eq. (61)) (μm)	t_{Al} (from Eq. (60)) (μm)	t_{Al} (from weight or supplier) (μm)
1	70.5	13930	2.3	2.3 ± 0.2	2.0 ± 0.1
2	206.9	39860	6.9	6.6 ± 0.5	5.0 ± 0.3
3	276.9	52660	9.2	8.7 ± 0.6	8.5 ± 0.4
4	331.7	62430	11.1	10.3 ± 0.7	10.2 ± 0.5
5	383.9	71530	12.8	11.9 ± 0.8	11.7 ± 0.7
6	680.7	119550	22.7	19.8 ± 1.4	19.3 ± 1.0

For the thinnest foil, foil #1, the energy loss ΔE is 70.5 keV and using S(2000 keV) = 29.93 keV/μm, the calculated thickness is 2.36 μm using the surface approximation (Eq. 61). This result is in very good agreement with that given by the foil supplier. It is seen that as the foil

thickness increases the surface approximation becomes less valid. Better agreement is obtained if changes in the stopping power are taken into consideration and used in a more exact calculation (Eq. 60).

As can be seen in Figure 24, the transmitted energy spectra become Gaussian-shaped and broader as the foil thickness increases (i.e. energy loss becomes larger). This effect is energy straggling, which arises from the statistical nature of the energy loss process. By fitting the experimental energy spectra (not including the long tails) with a Gaussian function to determine the standard deviation of the energy distributions, one can extract the contribution of the energy loss straggling in the foil from other energy degrading contributions (such as detector energy resolution, or geometrical effects).

The Bohr theory of energy straggling [15] yields the equation:

$$\Omega_B^2 = 0.26 Z_1^2 Z_2 Nt\left[10^{18}\, at/cm^2\right] \tag{63}$$

Where Ω_B is the energy standard deviation and Nt is the target areal density. The standard deviation Ω relates to the FWHM δE through the relation:

$$\delta E = 2.355\Omega \tag{64}$$

Example: Using Eqs. (63) and (64), 2 MeV protons transmitted through 10 μm Al have a FWHM δE of approx. 33 keV.

The measured experimental energy width δE_{exp} is comprised of all the different energy broadening effects added together in quadrature. For an ideal foil:

$$\delta E_{exp}^2 = \delta E_0^2 + \delta E_B^2 + \delta E_{det}^2 \tag{65}$$

Where δE_0 is the width of the incident proton beam, δE_B the Bohr straggling width and δE_{det} the detector energy resolution (a few keV). Experimental values obtained for δE_B from Eq. (65) are compared with the Bohr formula Eqs. (63) and (64), and are given in Table 21.

TABLE 21. EXPERIMENTAL AND CALCULATED BOHR ENERGY STRAGGLING

Al thickness (μm)	δE_B (experimental) keV FWHM	δE_B (calculated) keV FWHM
2.3 ± 0.2	20.0	16.2
6.6 ± 0.5	38.9	27.5
8.7 ± 0.6	51.8	33.4
10.3 ± 0.7	53.7	36.4
11.9 ± 0.8	66.5	40.0
19.8 ±1.4	78.5	55.5

Bohr straggling in Eq. (63) depends on the target thickness, but not on the ion energy. This description is valid in cases where the energy loss of ions in the target is large enough that the energy distribution can be described by a Gaussian shape, and small energy loss compared to the incident energy, i.e. when $0.01 < \Delta E/E < 0.2$. This condition is fulfilled for all foils except foil #6. From Table 21 it is seen that the experimentally obtained values for energy straggling are up to 60% larger than values predicted by Bohr's theory in the region where Bohr's theory should be valid (foils #1 - #5). Other theories were developed within the energy validity

region of the Born approximation such that of Livingston and Bethe [16], but they are not considered here. The difference between experiment and theory can partly be due to other effects arising from differences between a perfect foil and a real foil, such as material inhomogeneity and surface roughness, and other energy degrading terms not included in Eq. (65).

4.1.3. Recommended equipment

- A sample holder in front of the particle detector to hold thin foils for stopping power measurements;
- Thin foils of known areal density;
- A thin high-Z foil for scattering proton beam into detector;
- A particle detector placed at front angles and corresponding electronic chain with multichannel analyser;
- SRIM or SIMNRA software.

Thin foils are very fragile and should be handled with care to avoid breakage. Evacuating the vacuum chamber quickly with a rotary vacuum pump can cause a fast movement of air which also can break the foils. The roughing evacuation should be done slowly.

4.1.4. Safety precautions

The proton beam can produce high yields of X rays from collimators and beam-defining apertures if high currents are used and large amounts of the proton beam are incident on these beam trajectory defining components. A radiation survey should be made prior to undertaking measurements and if necessary, use the appropriate shielding and working distance to minimise any potential exposure risks.

4.2. NON-RUTHERFORD SCATTERING NEAR THE $^{12}C(p,p)^{12}C$ RESONANCE ENERGY

At ion energies above the Coulomb barrier, cross-sections for elastic backscattering are strongly dependent on ion energy, and deviate significantly from the classical Rutherford formula. For the elastic scattering reaction $^{12}C(p,p)^{12}C$ there is a resonance in the cross-section with peak maximum positioned at 1734 keV and FWHM of ~ 40 keV. As non-Rutherford cross-sections can be much higher (in some cases up to 100 times) than Rutherford ones, this can be utilised in practical applications to increase the analytical sensitivity of the backscattering technique. The intense resonance for ^{12}C or ^{16}O with helium ion beam is a commonly-used tool for depth-profiling carbon and oxygen in various substrates [17, 18].

4.2.1. Theoretical background

In this experiment, the yield of protons backscattered from a thin carbon foil is measured as a function of the proton energy (calculated from the magnetic field of the analysing magnet) in the energy range from 1610–1810 keV. The cross-section is calculated from the yield measurements.
The differential cross-section for backscattered protons at a scattering angle θ is given by Eq. (66):

$$\frac{d\sigma_C}{d\Omega}\left(E-\frac{\Delta E_C}{2},\theta\right)=\frac{A_C}{Q\Omega(\theta)N_C} \tag{66}$$

Where E is incident proton energy, ΔE_C is energy loss in the carbon film, A_C is the area under the carbon peak (yield), Q is the number of incident protons, $\Omega(\theta)$ the detector solid angle and N_C the number of carbon atoms per unit area (atoms/cm^2). The energy loss of protons ΔE_C in the 20 μg/cm^2 carbon foil used in this experiment was calculated using SRIM [14] as ~4 keV. The energy of the protons in the carbon foil is taken as that at the middle of the foil.

4.2.2. Experimental procedure

Figure 25 shows the experimental geometry. The measurements must be carried out in a vacuum chamber. The chamber should be light tight as the charged particle detector is sensitive to light (when bias is applied). A collimated proton beam with energy varied from 1600 to 1800 keV is incident on a thin carbon foil (10-20 μg/cm^2). A particle detector is placed at a backward angle (135°-170°) to detect the backscattered protons. The proton beam transmitted through the carbon foil is collected in a reliable Faraday Cup. The backscattering yield for the ^{12}C(p,p)^{12}C reaction is measured between 1610 keV and 1810 keV in steps of 10 keV.

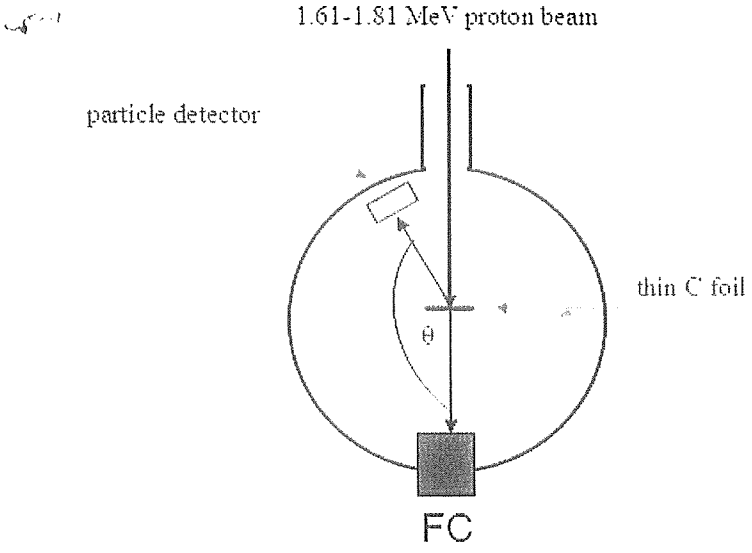

FIG. 25. Experimental setup for backscattering of protons from the 20 μg/cm^2 carbon foil.

All spectra are collected to the same number of incident particles i.e. to the same collected charge in the Faraday Cup (Q = 0.5 μC in this case). It is important that the target is as thin as possible to avoid the broadening of the narrow resonance. In this case, the energy loss of 1610–1810 keV protons in a 20 μg/cm^2 carbon is ~ 4 keV, which is 10% of the resonance FWHM. The spectrum of protons backscattered from the carbon foil for several proton energies is shown in Figure 26. It is clear that yield is very sensitive to the incident proton energy.

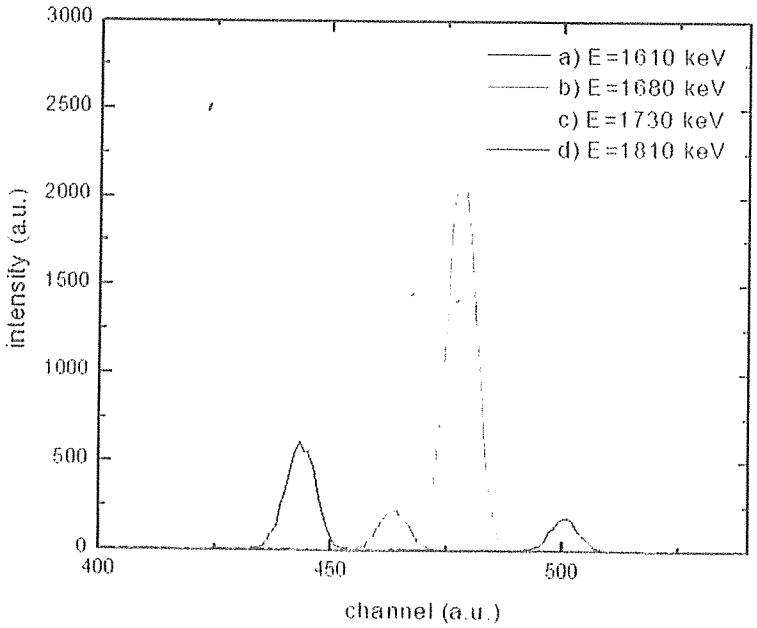

FIG. 26. Backscattering spectra of protons from a thin carbon foil for several incident energies: a) 1610 keV, b) 1680 keV, c) 1730 keV and d) 1810 keV. All spectra are normalised to the same number of incident protons (Q = 0.5 μC).

If the solid angle of particle detector is not known, absolute cross-section values cannot be calculated and only relative cross-section values obtained. The solid angle can be determined from a backscattering spectrum of heavy element such as Au, W, etc. for which cross-sections are pure Rutherford. For this system, $\Omega(\theta)$ is (7.6 ± 0.3) msr. For 0.5 μC the number of incident particles is 3.125×10^{12} protons. N_c for 20 μg/cm^2 carbon foil is 1000×10^{15} at/cm^2.

The measured differential cross-sections for $^{12}C(p,p)^{12}C$ scattering at 165° are shown on Figure 27 together with the evaluated cross-sections using SigmaCalc program from IBANDL [19], and cross-sections calculated using the Rutherford formula. The data is tabulated in Table 22. It can be seen that the Rutherford cross-section is completely erroneous for this reaction. Also, the present measurements are energy-shifted ~8 keV towards higher energies and could be attributed to a small inaccuracy in the accelerator energy calibration.

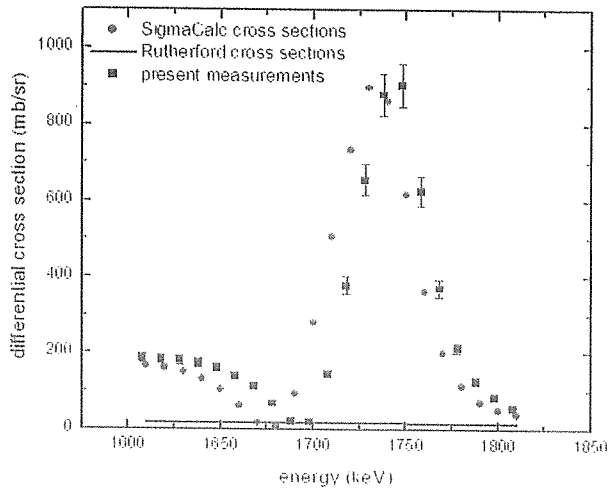

FIG. 27. Differential cross-sections for proton scattering from carbon at 165°.

The evaluated cross-sections are those obtained from the parameterisation of all the available experimental data for this reaction in the framework of nuclear physics models to obtain a set of best and recommended cross-section values. According to SigmaCalc, the cross-section resonance maximum is at 1734 keV.

The uncertainty in the calculated cross-section is ~ ± 7%, arising from:

- the statistical errors of the number of counts (peak areas) for backscattered protons;
- charge collection error 2%;
- solid angle determination 3%;
- target thickness 5%.

TABLE 22. DIFFERENTIAL CROSS-SECTIONS FOR $^{12}C(p, p)^{12}C$ AT 165°, MEASURED VALUES, SigmaCalc AND RUTHERFORD VALUES

E (keV) experimental	A_c	σ (mb/sr) present measurements	E (keV) tabulated	σ (mb/sr) SigmaCalc	σ (mb/sr) Rutherford
1608	4875 ± 70	186 ± 12	1610	167	18.4
1618	4793 ± 79	183 ± 12	1620	161	18.1
1628	477 0± 69	182 ± 12	1630	151	17.9
1638	4570 ± 68	174 ± 11	1640	133	17.7
1648	4241 ± 65	162 ± 10	1650	105	17.5
1658	3683 ± 61	140 ± 9	1660	64	17.3
1668	2978 ± 55	114 ± 7	1670	18	17.1
1678	1801 ± 43	69 ± 5	1680	8	16.9
1688	556 ± 25	21 ± 2	1690	95	16.7
1198	520 ± 23	20 ± 2	1700	281	16.5
1708	3846 ± 62	147 ± 9	1710	508	16.3
1718	9959 ± 100	380 ± 24	1720	735	16.1
1728	17217 ± 131	656 ± 41	1730	898	15.9
1738	23071 ± 152	879 ± 55	1740	862	15.7
1748	23740 ± 152	904 ± 56	1750	618	15.6
1758	16473 ± 129	628 ± 39	1760	364	15.4
1768	9751 ± 99	372 ± 23	1770	202	15.2
1778	5640 ± 76	215 ± 14	1780	116	15.0
1788	3331 ± 58	127 ± 8	1790	72	14.9
1798	2202 ± 47	84 ± 5	1800	51	14.7
1808	1445 ± 39	55 ± 4	1810	41	14.5

4.2.3. Recommended equipment

- A sample holder with thin self-supporting carbon foil;
- A particle detector placed at any backscattering angle (135–170°);
- A preamplifier, bias supply, spectroscopy amplifier, ADC and MCA;
- SRIM.

Thin foils are very fragile and should be handled with care to avoid breakage. Note, that evacuating the vacuum chamber quickly with a rotary vacuum pump can cause a fast

movement of air which also can break the foils. The roughing evacuation should be done slowly.

4.2.4. Safety precautions

The proton beam can produce high yields of X rays from collimators and beam-defining apertures if high currents are used and large amounts of the proton beam are incident on these beam trajectory defining components. A radiation survey should be made prior to undertaking measurements and if necessary, use the appropriate shielding and working distance to minimise any potential exposure risks.

4.3. MEASUREMENT OF THE HYDROGEN CONCENTRATION IN THIN FILMS

The hydrogen content and depth profile in materials can be measured using the Elastic Recoil Detection Analysis (ERDA) method. In this method, an ion beam with mass greater than hydrogen (e.g. ^{4}He, ^{7}Li, ^{12}C ions) is used in a two-body collision to knock hydrogen atoms in a forward direction. The knocked-on hydrogen atoms and forward scattered ion beam are incident on a charged particle detector placed at a forward angle. A stopping foil is placed in front of the charged particle detector to stop the scattered ion beam and transmit the knocked-on hydrogen atoms. Heavy ions have larger stopping powers than protons, allowing the thickness of the stopping foil to be tailored to stop the heavy ions yet transmit the recoiled protons. In this experiment, the hydrogen content in a thin foil of the polycarbonate material Mylar™ will be measured and compared with that of 36 at.% from its known stoichiometry $C_{10}H_8O_4$.

4.3.1. Theoretical background

The experimental geometry is shown in Figure 28. A heavy ion beam of several MeV energy (in this experiment 10 MeV $^{12}C^{3+}$ ions) is incident on a polymer material such as Kapton™ ($C_{22}H_{10}N_2O_5$) or Mylar™ ($C_{10}H_8O_4$). Two possibilities for the positioning of the target exist as shown in Figure 28. For thin transmission targets and in cases when one wishes to measure the total amount of H, the transmission geometry as shown in Figure 28a) can be applied. For thin hydrogen containing layers on a thick substrate, and in cases when the depth distribution of hydrogen in the sample is to be measured, the target should be tilted as shown in Figure 28b) and reflection geometry should be used.

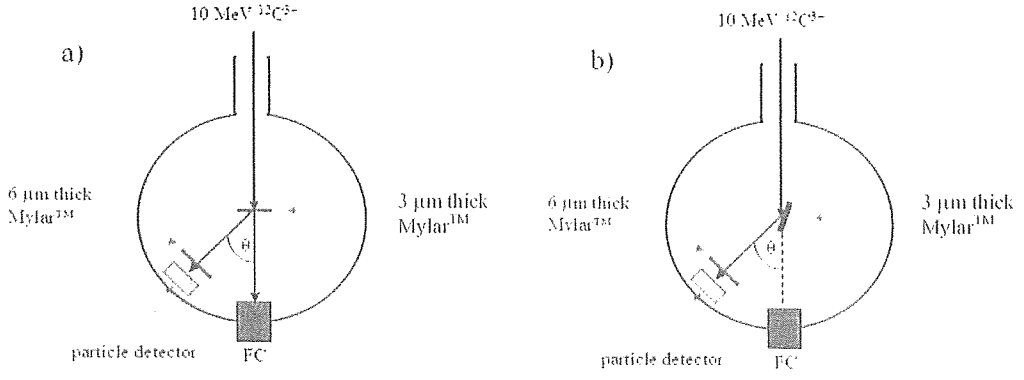

FIG. 28. Two possible configurations for the measurement of hydrogen content in the thin foil a) transmission and b) reflection geometry.

This experiment uses the transmission geometry shown in Figure 28a with the reaction kinematics shown in Figure 29.

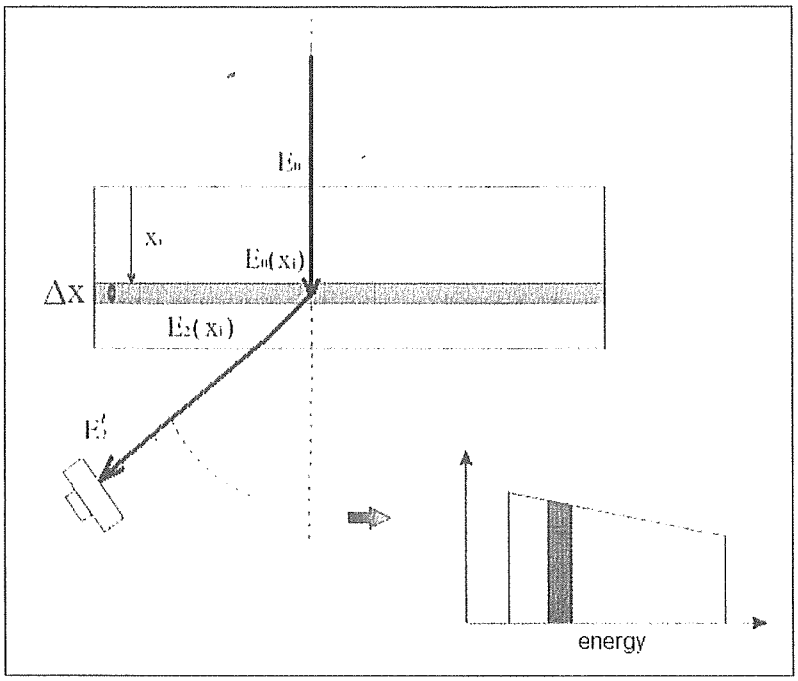

FIG. 29. Schematic presentation of the transmission geometry and idealised measured ERDA energy spectrum.

The incident ion beam with atomic number Z_1, mass M_1 and energy E_0 enters the sample under angle α (in our case and transmission geometry $\alpha=0$). At depth x_i, the incident ion has energy $E_0(x_i)$ given in Eq. (67):

$$E_0(x_i) = E_0 - \int_0^{x_i} \left(\frac{dE_0(x)}{dx} \right)_{in} dx \tag{67}$$

Where $\frac{dE_0(x)}{dx}$ is the stopping power of the ion beam in the sample.

At this depth x_i and energy $E_0(x_i)$, the incident ions recoil atoms j with atomic number Z_2 and mass M_2 into the solid angle $\Delta\Omega$ and angle β. The yield of recoiled atoms Y from this sub-layer Δx is given by Eq. (68):

$$\frac{dY}{dx}\Delta x = Q\Delta\Omega \frac{d\sigma(\overline{E}_0(x_i),\beta)}{d\Omega}\Delta x n_j \tag{68}$$

Where Q is the number of incident ions, n_j is atomic density of j atoms in the target, $\Delta\Omega$ is the solid angle, and $\frac{d\sigma(\overline{E}_0(x_i),\beta)}{d\Omega}$ is the differential cross-section for recoil of mass M_2 at energy $\overline{E_0}(x_i)$ in the layer Δx at x_i. In this experiment, the incident ion beam is ^{12}C and so the differential cross-section is described by the Rutherford formula Eq. (69):

$$\frac{d\sigma(\bar{E}_0(x_i),\beta)}{d\Omega} = \frac{\left[Z_1 Z_2 e^2 (M_1 + M_2)\right]^2}{\left[2M_2 \bar{E}_0(x_i)\right]^2 \cos^3 \beta} \tag{69}$$

Note: If using alpha particles as the ion beam, the cross-section is non-Rutherford!

In the two-body collision of an incident ion of mass M_1 with an atom of element j (mass M_2), the energy of the recoiled atom $E_2(x_i)$ is the kinematic factor K_{ERDA}:

$$E_2(x_i) = K_{ERDA} E_0(x_i) = \frac{4M_1 M_2 \cos^2 \beta}{(M_1 + M_2)^2} E_0(x_i) \tag{70}$$

The recoiled atoms lose energy as they travel through the sample, and exit with energy $E'_2(x_i)$ given by Eq. (71):

$$E'_2(x_i) = E_2(x_i) - \int_{x_i}^{d} \frac{1}{\cos\beta} \left(\frac{dE_2(x)}{dx}\right)_{out} dx \tag{71}$$

Where d is the total sample thickness and $\left(\frac{dE_2(x)}{dx}\right)_{out}$ is the stopping power of the recoiled ion on the way out from the target. A stopping foil is placed in front of the detector which has a thickness x_{foil}, chosen to just stop the incident ^{12}C ion beam at its primary energy E_0. Thus, the energy of the recoiled hydrogen atoms measured by the charged particle detector $E'_2(x_i)_{det}$ is given by Eq. (72):

$$E'_2(x_i)_{det} = E'_2(x_i) - \int_0^{x_{foil}} S_{foil}(E)\, dE \tag{72}$$

Where $S(E)_{foil}$ is the stopping power of the recoiled ions in the stopper foil. The resulting idealised spectrum for a thin homogenous sample with constant hydrogen distribution is shown in Figure 29.

4.3.2. Experimental procedure

The measurements must be carried out in a vacuum chamber. The chamber should be light tight as the charged particle detector is sensitive to light (when bias is applied). In this experiment a collimated beam of 10 MeV $^{12}C^{+3}$ ions was used to recoil hydrogen atoms from a (2.9 ± 0.1) μm thick Mylar™ foil in transmission geometry (Figure 28a). The charged particle detector was placed at 45° forward angle with the measured ERDA spectrum shown in Figure 30. This figure shows the spectrum obtained (a) when no stopping foil is placed in front of the particle detector and (b) with a stopping foil. With no stopping foil, the spectrum contains overlapping spectra from recoiled hydrogen, oxygen and carbon ions together with scattered carbon ions. A 6 μm thick Mylar™ foil used as the stopping foil in front of the particle detector clearly removes all ions except hydrogen. It can be also seen that hydrogen peak is shifted towards the lower energies in spectrum due to the energy loss of hydrogen ions in the foil. In both cases, the spectra were collected to the same number of incident particles i.e. to the same collected charge ($Q = 0.1$ μC).

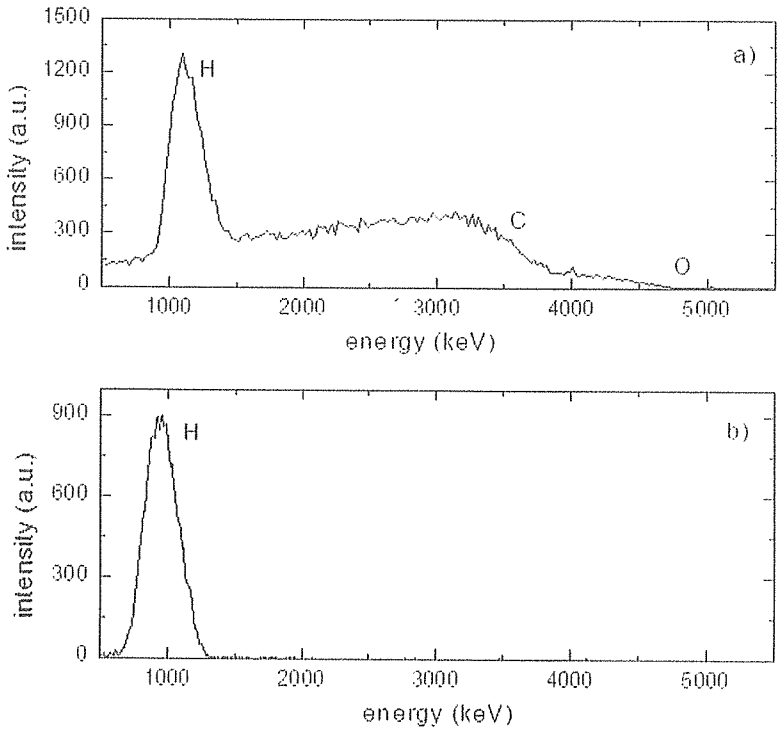

FIG. 30. Top: Spectrum of 10 MeV ^{12}C ions scattered from Mylar together with recoiled C, O and H ions from the target (without foil in front of the particle detector); Above: Spectrum of recoiled H atoms when 6 μm thick Mylar foil is placed in front of the particle detector.

The concentration of hydrogen atoms n_H in the Mylar™ foil can be calculated using Eqs. (67)-(69). If the sample is thick enough such that the energy loss of incident ions in the target cannot be neglected, as it is in this case, the calculation can proceed more easily by sub-dividing the thick sample into several thin slabs, and approximating the continually changing energy of the incident ion beam to be a constant in each of the slabs.

In this experiment, the thickness d of Mylar™ foil is ~28000×10^{15} at/cm^2. The total energy loss of 10 MeV C ions in this foil was calculated to be 2985 keV using SRIM [14]. The sample is divided into 10 slabs, each slab with thicknesses of $\Delta x = 2800\times10^{15}$ at/cm^2. The yield of hydrogen atoms from each slab with a thickness Δx can be calculated by using the cross-section at the mean energy in the slab. The differential cross-section $\frac{d\sigma(\bar{E}_0(x_i),45^\circ)}{d\Omega}$ used for calculation in each slab is tabulated in Table 23. The values have been calculated by the utility subroutines incorporated into SIMNRA [20].

The total yield of hydrogen ions is obtained by summing the yields from all 10 slabs. The hydrogen depth profile is coarsely represented by the concentrations calculated for each slab.

TABLE 23. CROSS-SECTIONS USED TO CALCULATE YIELD OF RECOILED HYDROGEN IONS IN EACH SUBLAYER IN THE MYLAR™ SAMPLE

x_i (10^{15} at/cm^2)	$E_0(x_i)$ (keV)	ΔE (keV)	$\overline{E}$ (keV)	$\frac{d\sigma}{d\Omega}(\overline{E},45°)$ (mb/sr)
0	10000	283	9859	904
2800	9719	286	9574	958
5600	9431	288	9287	1018
8400	9143	291	8998	1085
11200	8852	294	8705	1159
14000	8558	296	8410	1242
16800	8262	299	8112	1335
19600	7963	302	7807	1441
22400	7661	304	7509	1557
25200	7357	307	7204	1692

As we wish to obtain a bulk-averaged hydrogen concentration in the Mylar™ film, the experimentally obtained total hydrogen yield is taken from spectrum that is shown in Figure 30b. The yield Y is the area under the peak (22640 counts). The total collected charge was 0.1 μC which for q=+3 charge state, corresponds to 2.08×10^{11} incident carbon ions. The solid angle of the particle detector at 45° is Ω= (8.76 ± 0.26) msr. If the solid angle of the particle detector is not known, it can be determined from a forward scattering spectrum of protons from some other thin transmission foil of heavy element such as Au, Cu, Ni, etc. for which cross-sections are Rutherford.

The bulk-averaged atomic concentration of H atoms in Mylar™ sample is calculated using Eq. (68) which is:

$$n_H = \frac{Y}{Q\Omega \sum \frac{d\sigma}{d\Omega}(\overline{E_0}(x_i),\beta)\Delta x}$$

$$= \frac{22640}{2.08\times10^{11}\cdot 8.76\times10^{-3}sr\cdot 2800\times10^{15}at/cm^2\cdot 12391\times10^{-27}cm^2} = 0.3579$$

This result is in excellent agreement with the atomic concentration of hydrogen in Mylar™ obtained from its well-known stoichiometry $C_{10}H_8O_4$:

$$n_H = \frac{8}{10+8+4} = 0.3636$$

4.3.3. Concluding remarks

ERDA spectroscopy is very efficient technique using small accumulated charges (0.1 μC), and due to high recoil cross-sections, high yields can be obtained. By using a simple stopping foil, the unwanted background due to scattering events can be eliminated and the sensitivity for hydrogen detection enhanced. Analytical codes such as SIMNRA [20], NDF [21] or RUMP [22] are useful programs that can simulate elastic scattering experiments in various geometries (including RBS and ERDA) and are routinely used to obtain concentrations as well as depth profiles of unknown elements in the sample from the experimental spectrum.

Radiation induced damage occurs in polymeric materials and numerous other hydrogen containing materials in which hydrogen is lost during the measurements. The hydrogen loss can be significant and depends on many parameters such as ion type, ion current or total collected ion dose on the sample. To minimise losses, it is recommended to keep beam currents low, to have a large solid angle for the charged particle detector, and to keep the measurement charge low, measuring only until sufficient statistics have been collected under the hydrogen peak.

4.3.4. Recommended equipment

- A particle detector positioned at forward angle with stopper foil;
- A preamplifier, bias supply, spectroscopy amplifier, ADC and MCA;
- Reliable charge integration;
- A thin target foil with well-known stoichiometry and hydrogen concentration;
- SRIM;
- An ion beam with mass >1. Helium (~2 MeV) or carbon beams are most commonly used.

4.3.5. Safety precautions

The proton beam can produce high yields of X rays from collimators and beam-defining apertures if high currents are used and large amounts of the proton beam are incident on these beam trajectory defining components. A radiation survey should be made prior to undertaking measurements and if necessary, use the appropriate shielding and working distance to minimise any potential exposure risks.

4.4. PROTON-INDUCED GAMMA RAY EMISSION ANALYSIS OF Na AND Al

When a beam of particles hits the sample surface layer, nuclear reactions are induced, and gamma radiation is emitted. In PIGE, the radiation is detected during irradiation (prompt gamma emission instead of activation). The PIGE method is used in similar way as the PIXE method. PIGE enables the detection of the light elements with good sensitivity. The use of different bombarding particles and energies offers varying sensitivity for different elements, which makes this technique trickier to use than the PIXE method. The common bombarding particles used in PIGE analyses are protons, deuterons and alpha-particles. In this experiment, protons are employed for detection of aluminium and sodium.

4.4.1. Theoretical background

The observed gamma ray yield (or interaction products in general) is directly dependent on the cross-section (which defines the probability of a specific type of interaction) and the density of atoms of the kind to be determined. For thick samples (sample thickness greater than the incident ion range) and provided that the product radiation is not significantly attenuated when passing through the rather thin layer to the detector, the observed yield may be expressed as:

$$Y_i = n \varepsilon f_{wi} \int_0^{E_a} \sigma_i(E) / S_m(E) dE \qquad (73)$$

Where i is the measured nuclide, m the matrix, n the number of bombarding particles, ε the detection efficiency including the solid angle, E_p the incident ion energy, f_{wi} the weight fraction of nuclide i, S_m the stopping force (or stopping power) for the matrix, and $\sigma_i(E)$ the cross-section for the specific reaction. In addition, we assume that the nuclide to be measured is evenly spread through the matrix. Also, straggling effects are ignored and smooth cross-section curves without resonance structures are assumed.

The complicating factors are that accurate cross-section data are not always available (within the energy region from incident energy to zero) and that the major element composition of the sample is needed to calculate the stopping forces.

An advantage of the method is that the gamma ray peaks are generally well isolated, and the energy is high enough that absorption corrections are not needed. The high penetrability of the gamma rays also simplifies the experimental arrangements.

The available literature for absolute thick-target gamma ray yields (per solid angle in steradians, and microCoulombs of collected charge) have been collected [23]. In several studies, the atlas of appropriate gamma ray spectra for light elements is also provided.

Detailed prescriptions for light element analyses by particle-gamma reactions may be found in the IBA Handbook [23]. Additionally, several important factors (e.g. geometry, background and interferences as well as peak broadening effects) to be taken into account for accurate element analyses by the PIGE method are described in this reference and the reader should consult Refs [23, 24] for more in-depth discussion on the method details. In this experiment only analysis of aluminium and sodium is considered.

An advantage of PIGE is the high penetrability of gamma rays, thus diminishing matrix effects. The detector can be positioned immediately behind the sample, providing a maximum solid angle for improved sensitivity. The experimental setups are simple, and with external beams, the usability of the technique can be enhanced. As a rule, very small amounts of sample material are needed. Also, surface topography does not significantly influence the determinations. The technique is fast and non-destructive. Using PIGE in combination with other ion beam techniques, nearly all elements can be detected simultaneously. On the other hand, PIGE can be used only for the analysis of selected isotopes, and its sensitivity for many elements is only moderate. Because the optimal conditions, such as the bombarding particles and their energy, depend on the matrix and the isotope to be detected, no universal "best" conditions and physical parameter choices can be provided.

4.4.2. Use of standards

Concentrations of elements distributed homogeneously in thick samples can be obtained by comparison to standards. Many multi-element standards exist for the analysis of geological, biological, and medical samples [e.g., National Institute of Standards and Technology (NIST), Institute for Reference Materials and Measurements (IRMM), International Atomic Energy Agency (IAEA)]. In many cases proper standards can be prepared by mixing a known amount of the element to be determined into a matrix similar to the one being studied. For example, the determination of carbon, nitrogen, and oxygen can be carried out with organic compounds as standards. The known stoichiometry for C, N, and O of the compounds can be used directly. As a restriction, the selected organic compounds should not have very high concentrations of any single element (above about 40 wt%).

4.4.3. PIGE analysis of Na and Al

An experimental set-up consisting of a vacuum target chamber (alternatively an external beam set-up may be used) with appropriate charge integration possibility is shown in Figure 31.

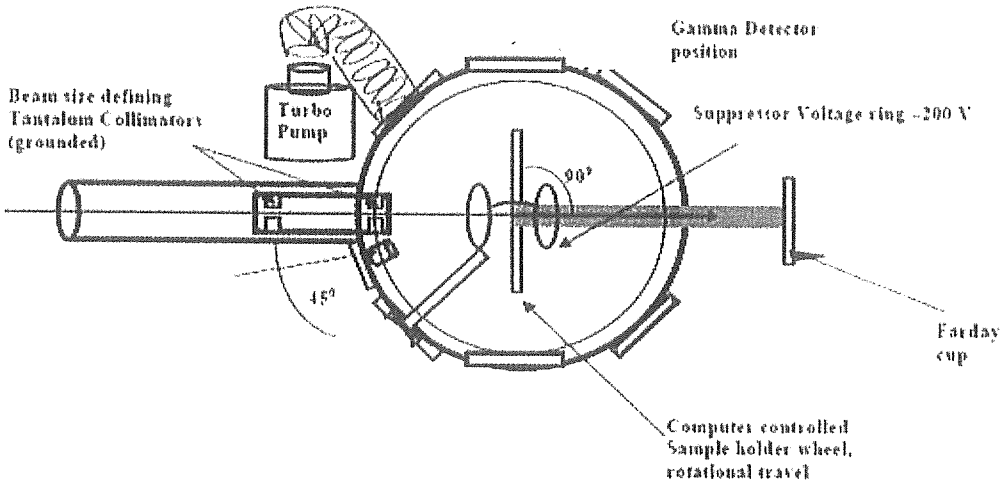

FIG. 31. Typical PIGE set-up used for in-vacuum measurements. In case of a thin sample the integrated charge can be collected from the Faraday cup. For thick samples the current integration is carried out directly from the sample.

The feasible gamma ray lines for elemental analyses of sodium and aluminium are discussed below.

Sodium has one stable isotope, ^{23}Na.
A good sensitivity for sodium analysis is obtained by detecting the 440 keV γ rays originating from the reaction ^{23}Na(p,p'γ)^{23}Na. The γ ray line at 1636 keV is somewhat Doppler-broadened.

Aluminium has one stable isotope, ^{27}Al.
Aluminium has several strong γ ray lines; at 844 keV and 1014 keV originating from the reaction ^{27}Al(p,p'γ)^{27}Al, at 1369 keV from the reaction ^{27}Al(p,αγ)^{24}Mg, and at 1779 keV originating from the reaction ^{27}Al(p,γ)^{28}Si (only at E_p<3 MeV). The 1369 keV line might have interference from sample magnesium. The 1779 keV line may contain interference from sample silicon and phosphorus. Also, the 844 keV and 1014 keV lines which are most suitable for aluminium analysis have interference from magnesium, ^{26}Mg(p,γ)^{27}Al, but fortunately the magnesium yields are rather low.

Typical gamma ray spectra obtained by 1.0 and 2.4 MeV proton bombardments of thick Na and Al samples are shown in Figures 32 and 33.

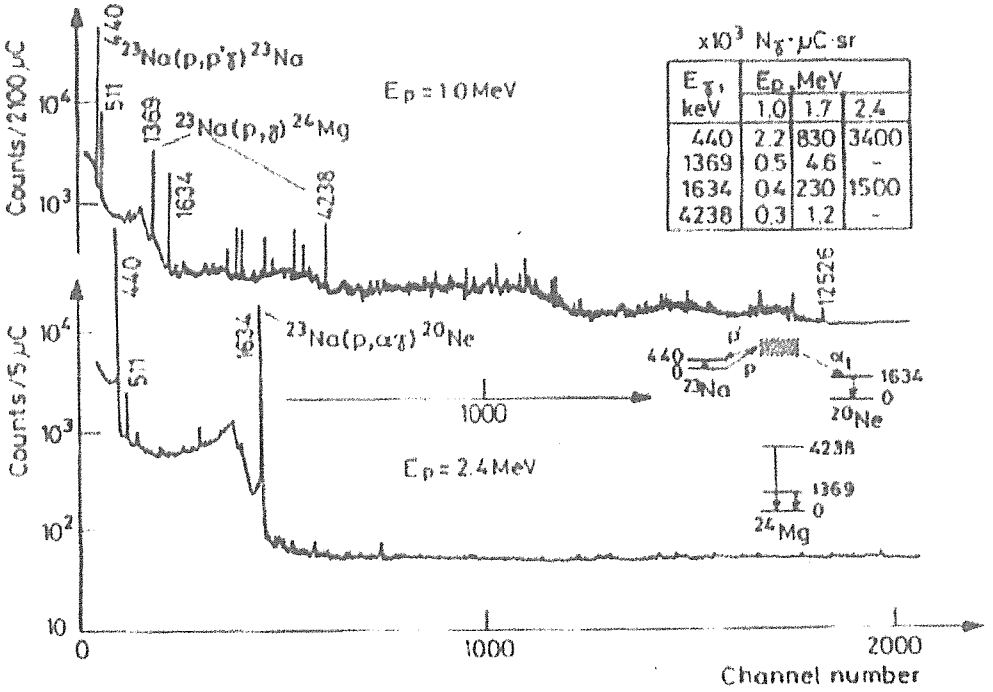

FIG. 32. Typical gamma ray spectra obtained from a thick sodium sample by 1.0 and 2.4 MeV protons. [25]

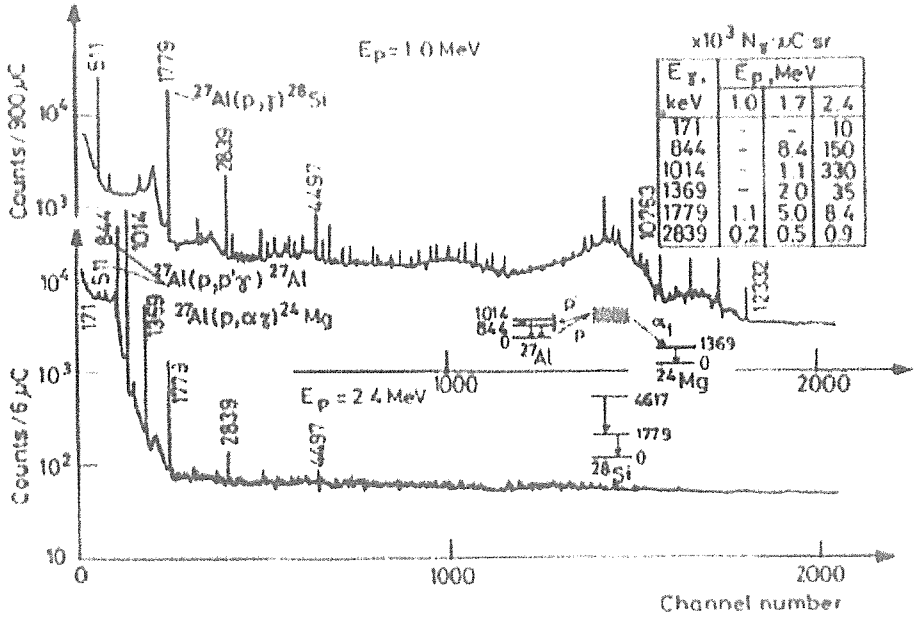

FIG. 33. Typical gamma ray spectra obtained from a thick aluminium sample by 1.0 and 2.4 MeV protons. [25]

4.4.4. Experimental procedure

(1) The standard sample and the "unknown" sample are bombarded with a proton beam of selected energy and the corresponding gamma ray spectra are recorded.
(2) The measurements should be normalised to correspond to the same collected charge.
(3) The calculated 440 keV and 844 keV peak area ratios (standard sample/"unknown" sample) and the concentrations stated in the standard sample certificate provide the Na and Al concentrations of the "unknown" sample. The deducted data can be collected in Table 24 to facilitate the analysis.
(4) For comparison determine the concentrations using the other gamma ray peaks (1636 keV for Na and 1014, 1369 and 1779 keV for Al). Be careful of possible interferences!
(5) Compare the obtained Na and Al concentration values with the certified values given in the "unknown" sample certificate.

TABLE 24. *DATA FOR Na AND Al CONCENTRATION DETERMINATION FROM AN "UNKNOWN" SAMPLE*

Sample	Collected charge [μC]	Na peak area [normalised by charge]	Al peak area [normalised by charge]	Au/As·Na-std.conc.	Au/As·Al-std.conc.
Standard (S)					
Unknown (U)					

4.4.5. Recommended equipment

- An energy calibrated gamma ray detector;
- Standard electronics for gamma ray spectroscopy;
- Peak fitting software;
- A 2-3 MeV proton beam, energy selected as available and most convenient;
- Two samples with known Na and Al concentrations. One is used as a standard and the other one as the "unknown" sample to be analysed. To check the accuracy of the obtained result, the concentration values should be compared with the values given in the "unknown" sample certificate.

4.4.6. Safety precautions

When energetic protons (above ~2 MeV) are used to bombard light elements (especially Li, Be, B) high neutron yields can occur as well as potentially high fluxes of high-energy gamma rays. The local accelerator related radiation safety rules and regulations must be followed to minimise the generation and exposure to any neutrons and high-energy gamma rays.

4.5. NUCLEAR REACTION ANALYSIS OF LIGHT ELEMENTS

Nuclear reactions induced by bombardment with energetic charged particles causing the emission of other energetic particles (particle-particle reactions) are used for elemental analysis. These methods are best applied to light elements, as nuclear reactions on light nuclei often have large Q-values and high cross-sections. The analysis method consists of the detection of charged particles produced by nuclear reactions during irradiation. In principle any reaction may be used, but with increasing projectile energy the number of outgoing channels becomes so large that the interpretation of the spectra from a complex sample becomes practically impossible. The most commonly used reactions are (p,α), (d,p) and (d,α). Alpha particle induced reactions have had limited use. Incident particle energies from 0.5 to 2 MeV are most useful for minimizing interference from reactions in heavy isotopes.

Bulk composition can be derived from particle-particle measurements assuming a homogeneous sample. The sensitivity is good for light elements, but for heavy elements, the Coulomb barrier reduces the cross-sections, thereby limiting the applications. Reaction cross-sections of 10 to 100 mb/sr are observed for proton and deuteron induced reactions in light isotopes (e.g. Li, Be, B). Sensitivities of the order of 10 μg/g or even less are possible with measuring times of the order of tens of minutes. Depth profiling of light elements is also feasible by this technique.

In this experiment, as an example, oxygen analysis via the $^{18}O(p,\alpha)^{15}N$ reaction is shown.

4.5.1. Theoretical background

The choice of optimum experimental parameters is an essential part of the design of an NRA measurement. Analysis using particle-particle reactions involves choices such as:

- choice of reaction;
- incident particle energy;
- detection angle.

Usually there is no analytical form of the nuclear cross-sections, so reliable experimental design and data analysis depends largely on the availability of measured cross-sections in the energy range and at angles of interest [19, 26].

The energy spectrum method is the main profiling technique used with particle-particle reactions. It is a relatively quick method since the necessary data are obtained during one irradiation with fixed incident particle energy. The product particle is usually different from the incident particle and higher in energy which has an important influence on the choice of experimental conditions and the performance achieved. Many variations of the method have been developed and the reader is asked to consult one of the references for more details.

NRA spectra are sometimes difficult to interpret as peaks of different particles (or the same particles with different energies) can overlap. Nuclear level diagrams showing nuclear structure and properties of nuclear levels can be found from the Nuclear Physics journal series [27].

Depth information is always obtained from the product particle spectrum if the depth exceeds that corresponding to the energy resolution. The energy interval to the next lower group in the spectrum sets the maximum depth that can be profiled. It should be noted that these

parameters are unique for each reaction. The maximum depth is usually limited to the order of 1 μm. At depths greater than approximately 100 nm, the effects of multiple scattering and energy loss straggling on both incident and product particles degrade the resolution.

4.5.2. Experimental procedure

Most particle-particle reaction measurements are made with very simple experimental arrangements. The basic NRA geometry is shown in Figure 34.

To avoid high count rate from elastically scattered primary particles, it is necessary to filter this large flux. The most common way to do this is to place a foil in front of the detector (absorber foil technique). The thickness of the foil should be equal to the range of the scattered particles so that these are absorbed while the higher energy reaction products pass through. Mylar or Kapton are common absorber foil materials. The major disadvantage of this absorber foil technique is that energy straggling takes place in the foil, resulting in poor energy resolution in the measured spectrum. As an example, the typical particle detector energy resolution of 10-15 keV may be degraded to 50-100 keV. This is not a problem if there is a sufficient energy difference between particle groups from different reactions or different target nuclides. Inhomogeneities in the absorber foil thickness affect the energy resolution.

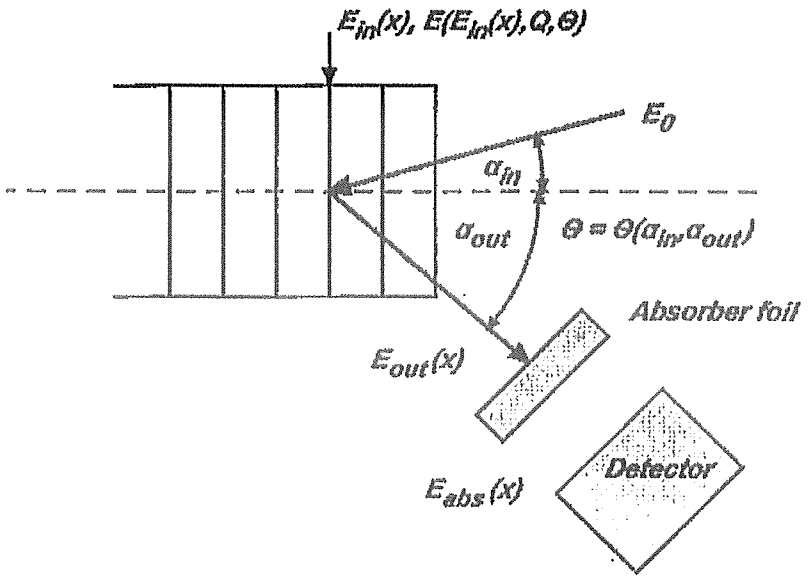

FIG. 34. Typical scattering geometry used in NRA experiments. E_o is the incident energy, E_{in} is the incident particle energy at reaction site, E_{out} is the reaction product energy after traversing out of the sample and E_{abs} is the particle energy after passing through the absorber foil. The conventional scattering angle is θ, which is the angle between the incident and exiting beams. The figure has been adopted from Ref. [23].

Practical information related to the detection of the light elements and a comprehensive list of proton and deuteron induced reactions feasible for light elements characterisation via particle-particle reactions is provided in Ref. [23].

The following brief list is only indicative and excludes reactions exhibiting simultaneous gamma ray and particle emission, as analyses based on detection of gamma rays are often more convenient than on detection of the charged particles.

TABLE 25. BRIEF LIST OF LIGHT ELEMENT NUCLEAR REACTION ANALYSIS

^{6}Li	the (d,α) reaction provides reasonable performance.
^{9}Be	the (p,α) reaction is useful for depth profiling.
^{11}B	the (p,α) reaction is useful for profiling and boron detection.
^{12}C	the (d,p) reaction is most used. It can be used for simultaneous C, N and O determinations in thin layers.
^{13}C	the (d,p) reaction can be used for carbon detection and C isotope ratio measurements.
^{14}N	the (d,p) and (d,α) reactions can be used.
^{15}N	the (p,α) reaction is useful.
^{16}O	the (d,p) reaction is most used for profiling purposes (simultaneous C, N and O analyses).
^{18}O	the (p,α) reaction utilizing narrow resonances is commonly used for depth profiling. The (d,p) and (d,α) reactions can also be used.
^{23}Na	the (p,α) reaction may be used for depth profiling.
^{28}Si	the (d,p) reaction can be used with reasonable sensitivity.
^{31}P	the (p,α) reaction gives the best sensitivity.
^{32}S	the (d,p) reaction has been used for sulphur determination and profiling.

4.5.3. Experiments and calculations

(1) A fixed proton energy between 500-700 keV is selected; these are the most commonly adopted energies.
(2) A detection angle θ of 165° is selected and fixed.
(3) Calculate the alpha particle energy as a function of incident proton energy (E_p) using Eq. (74), the kinematic formula for a two-body nuclear reaction, from initial proton energy downwards.

$$E_\alpha^{1/2} = B \pm (B^2 + C)^{1/2}, \tag{74}$$

Where $B = \frac{(M_p M_\alpha E_p)^{1/2}}{(M_\alpha + M)} \cos\theta$ and $C = \frac{\{MQ + E_p(M - M_p)\}}{(M_O + M)}$. M is the product nucleus mass. The Q-value for the reaction is 3.9804 MeV.

(1) Test (using the sample to be analysed) the effects of different absorber foil thicknesses and find the absorber foil thickness sufficient to exclude the scattered incident particles.
(2) Compare the adopted Mylar thickness value with the calculated value obtained by the SRIM program [14].
(3) Estimate the cut-off energy (for the selected absorber) for the emitted alpha-particles (by SRIM program).
(4) Using this value, estimate the approximate depth from which information is still obtainable (taking into account the energy loss of the alpha-particles in the sample material itself). First, based on calculations using Eq. (74), estimate the validity of using constant alpha-particle energy for this approximation.

(5) Measure the sample and note the obtained spectrum shape. Discuss the specific features according to the following points.

Notes:

- The measured alpha-particle energy depends on the energy loss of the protons when reaching depth x ($\alpha_{in} = 0$) and the energy loss of the emitted alpha-particles when traversing a distance x × sec α_{out} in the sample before reaching the detector. The alpha-particle energy thus specifies the depth. The highest energy corresponds to the nearest surface region.
- The number of alpha-particles with specific energy depends on the reaction cross-section at fixed proton energy. Since the ^{18}O concentration is constant, the shape of the spectrum should be closely related to the cross-section curve (Figure 35) (ignoring the effects of straggling and detector energy resolution).
- The easiest procedure for composition determination by NRA is to use a standard sample. This is feasible if the standard and the unknown sample are both bulk samples (measurements under same experimental conditions). Then the composition at the surface can be obtained by applying the surface-energy approximation.

4.5.4. Recommended equipment

The experimental arrangement required for particle-particle analysis is similar to that for RBS and is shown schematically in Figure 35.

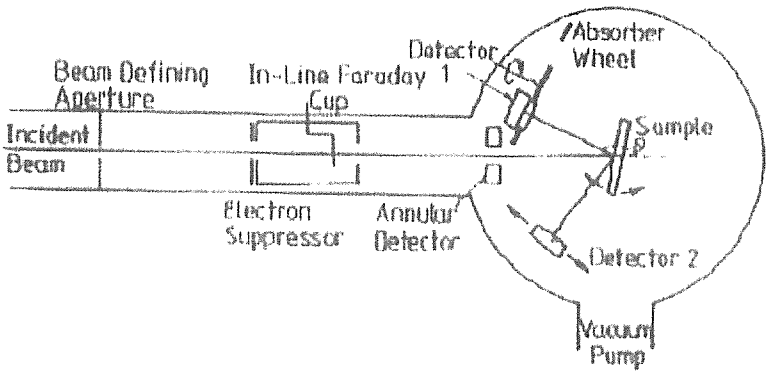

FIG. 35. Schematic layout of particle-particle analysis facility.

The experimental geometry consists of:

- A scattering chamber (light tight), with current integration;
- A particle detector with standard electronics for spectroscopy;
- Absorber foils of various thicknesses;
- A sample with constant oxygen concentration.

As an example of the use of particle-particle reactions for elemental analysis of light elements, the reaction $^{18}O(p,\alpha)^{15}N$ for oxygen determination is demonstrated. The straightforward method of using an absorber foil is employed. The relevant cross-sections as a function of proton energy are provided in Figure 36.

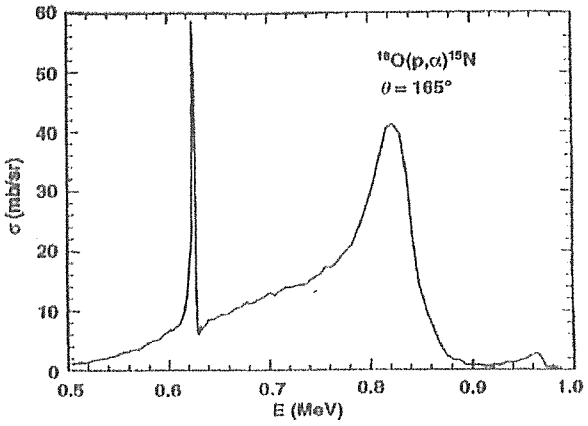

FIG. 36. Cross-sections of the $^{18}O(p,\alpha)^{15}N$ reaction at the indicated laboratory angle of 165°. Ref. [23].

4.5.5. Safety precautions

Even though charged particles are detected in this experiment it should be always kept in mind that energetic gamma rays and in some cases also neutrons are emitted during the sample bombardment. Specifically note that whenever deuterons are used as bombarding particles, a clear possibility for radiation hazard exists due to the high neutron yields. A radiation survey should be made prior to undertaking measurements and if necessary, use the appropriate shielding and working distance to minimise any potential exposure risks. In addition, whenever deuterons are used as bombarding particles and due to high neutron fields created, the surrounding metal structures can become activated increasing additional radiation risk. In such cases, continuous monitoring of neutron and gamma dose rate might need to be installed, and the entrance in the experimental room might be permitted only after decay of activation products.

4.6. RUTHERFORD BACKSCATTERING SPECTROMETRY OF HEAVY ELEMENT LAYERS ON A SILICON SUBSTRATE

Rutherford Backscattering Spectrometry (RBS) [28] is the most widely used ion beam technique. The technique is based on the determination of the number and energy distribution of particles backscattered from the sample atoms. The most common applications include the determination of sample stoichiometry, elemental areal density, and impurity depth profiling in thin films.

Presently many specific variations of RBS are used, such as:

- Heavy ion backscattering HIBS. This option provides improved mass and depth resolution;
- Utilisation of the ion channelling feature. This special feature is commonly used for the detection of displaced atoms in crystalline structures;
- Utilisation of non-Rutherford elastic scattering. This improves the sensitivity for several light element detection and profiling.

Several excellent presentations on the technique covering the principles and details are available. The reader should consult the list of references at the end of this experiment. In this experiment only the conventional use of RBS is treated and experimented via thin film stoichiometry and thickness determination.

4.6.1. Theoretical background

Only the main points related to the data analysis of this experiment are briefly discussed. Figure 37 shows the typical RBS geometry, the equations of ion transport and typical backscattering spectrum from a homogeneous single-element thick sample.

In the equations ε is the stopping cross-section factor and N is the atomic density of the sample material. H_o is the height (counts/channel) of the leading edge of an elemental peak corresponding to scattering from the sample surface. δE is the energy width per channel and ε_o is the surface-energy approximation of the stopping cross-section factor evaluated at the incident energy. $\sigma(E_o)$ is the scattering cross-section value at the incident energy. The other symbols are defined in the text below. Note that the equations above refer to a single-element sample.

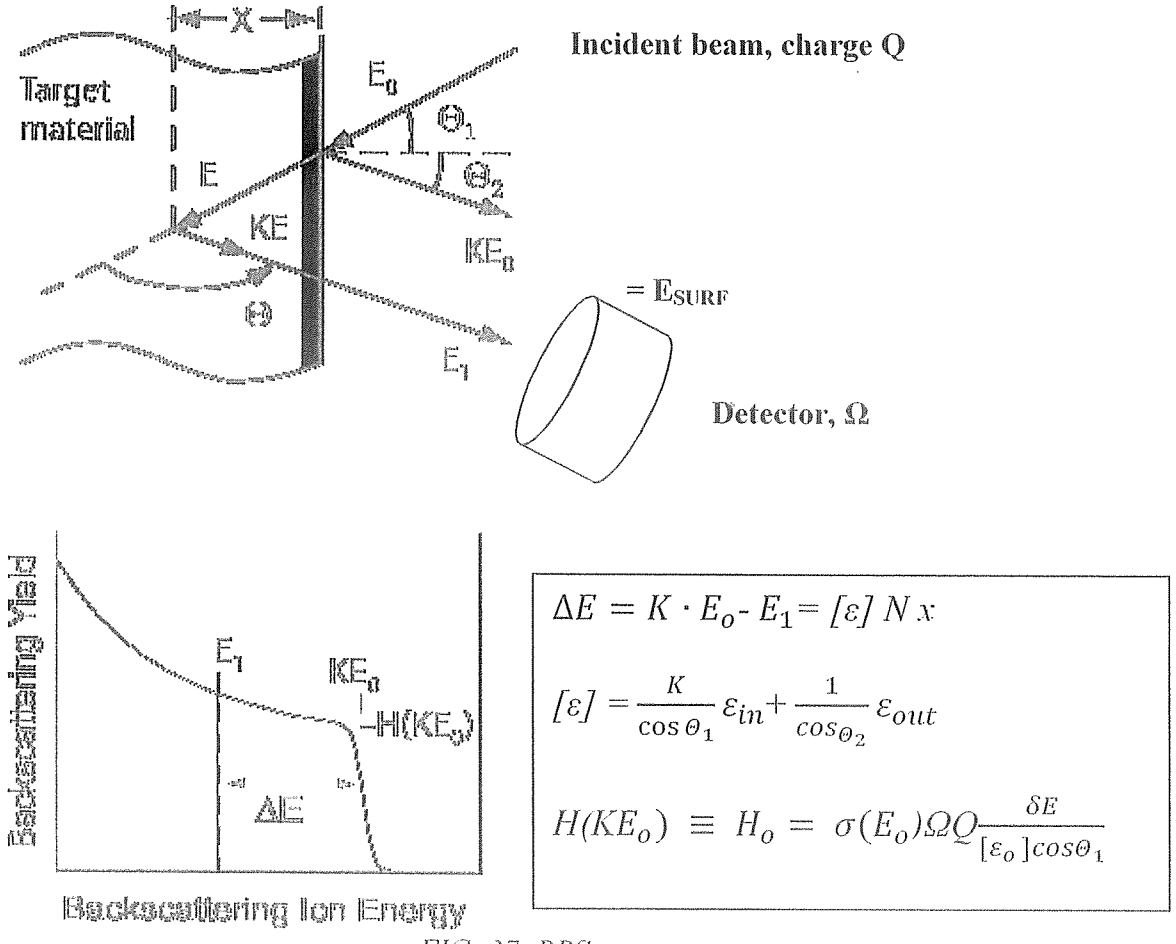

FIG. 37. RBS geometry.

The kinematic factor is the ratio of the scattered ion energy E_1^i (from element i) to the initial ion energy E_0.

$$K_i = \frac{E_1^i}{E_0} \tag{75}$$

From the conservation of energy and momentum applied to the two-body collision between isolated particles of masses M_1 (incident particle) and M_2 (target) we obtain:

$$K = \left[\frac{\left(M_2^2 - M_1^2 \sin^2\theta\right)^{1/2} + M_1 \cos\theta}{M_1 + M_2}\right]^2 \tag{76}$$

Where θ is the scattering angle in the laboratory system. As the other parameters are fixed, M_2 can be determined from this relation and the target element can be identified.

The areal density $(Nt)_i$ in atoms per unit area for element i is obtained by using the following equation:

$$(Nt)_i = \frac{A_i \cos\theta_1}{Q\Omega\sigma_i(E,\theta)} \tag{77}$$

The use of this equation requires knowledge of the detector solid angle (Ω), integrated peak count A_i, the collected charge Q and the Rutherford scattering cross-section $\sigma_i(E,\theta)$. θ_1 is the angle of incidence of the bombarding particles with respect to the sample normal. The Rutherford scattering cross-sections are calculated directly by the employed simulation programs used for the spectrum analysis. In Eq. (77) N_i is the atomic density (atoms per unit volume) of element i and t is the film thickness.

The average stoichiometric ratio for the sample film (A_mB_n) can be now calculated by using Eq. (77):

$$\frac{n}{m} = \frac{N_B}{N_A} = \frac{A_B}{A_A}\frac{\sigma_A(E,\theta)}{\sigma_B(E,\theta)} \tag{78}$$

Note that the result depends only on the ratios of the peak area counts and of the cross-sections. It is not dependent on the collected charge or the detector solid angle which are clearly more difficult entities to be determined accurately.

Conversion of $(Nt)_i$ to thickness t requires information on the film density (ρ_{AB}). The atomic densities N_A^{AB} and N_B^{AB} can then be obtained from:

$$N_A^{AB} = \frac{m\rho_{AB}N_o}{M_{AB}} \quad \text{and} \quad N_B^{AB} = \frac{n\rho_{AB}N_o}{M_{AB}} \tag{79}$$

Where N_o is Avogadro's number and $M_{AB} = mM_A + nM_B$ is the molecular weight of the compound A_mB_n.

From Eq. (77) we obtain the film thickness:

$$t = \frac{(Nt)_A}{N_A^{AB}} = \frac{(Nt)_B}{N_B^{AB}} \tag{80}$$

The factors $(Nt)_i$ are obtained from Eq. (77) and the atomic densities N_i^{AB} from Eq. (79).

4.6.2. Experimental procedure

The employed set-up is similar to the one used for nuclear reaction analysis described in experiment 4.5. Typical arrangements are shown in Figures 35 and 38.

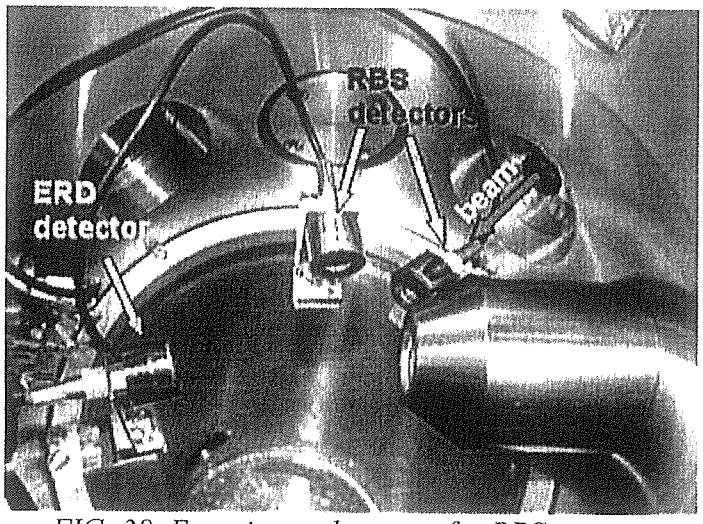

FIG. 38. Experimental set-ups for RBS measurements.

Two detection geometries are commonly used. They are referred to as the IBM and Cornell geometries. The incident beam is always horizontal and the sample surface is vertical. In the IBM geometry the detector is also placed in the same horizontal plane. In the Cornell geometry the detector is placed directly below the incident beam. For both arrangements, the charged particle detector is placed at a backward angle (e.g. 170°). The most typical particle beam for conventional RBS measurements is a ^{4}He beam with energy of 1-2 MeV. A very basic energy spectrometry system for charged particle detection is employed, as shown in Figure 39. Thin film samples are prepared e.g. by the Atomic Layer Deposition (ALD) method, and are characterised by the RBS technique. In this experiment a two component thin film sample on a silicon backing is measured and analysed (here a Sn_xBi_y thin film grown on silicon substrate was chosen to demonstrate the spectrum analysis, but in fact any thin film sample available will do).

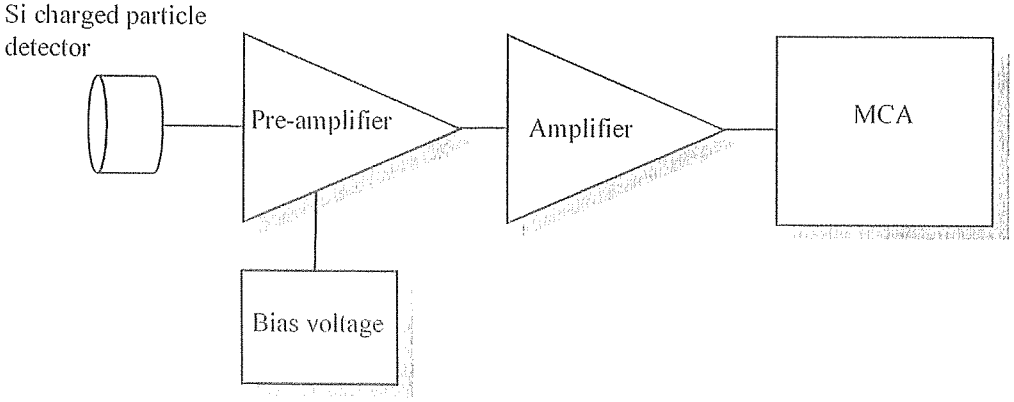

FIG. 39. Detection system used in conventional RBS measurements.

4.6.3. Energy calibration

The energy of the detected particles is converted to a charge pulse and after suitable amplification to a voltage pulse. The height of the analogue voltage pulse is converted further to the digital output of the ADC (channel number). The energy E of the detected particle is linearly proportional to the channel number ch of the MCA:

$$E = k_{ch} \times ch + E_0 \tag{81}$$

Where k_{ch} (energy/channel) and E_0 (zero offset) are the energy calibration coefficients. These parameters are needed for the evaluation of the spectra or for fitting a theoretical spectrum to the experimental one. In RBS analysis the energy of the particles scattered from known surface elements can be calculated. Therefore, one can use standard samples with known elements at the surface for energy calibration. From the position of the surface peaks (very thin films) or steps (thick samples) and the corresponding energy values, the calibration coefficients (k_{ch} and E_0) are then evaluated through linear regression.

4.6.4. Measurements

Accurate ^{4}He ion beam energy can be determined by employing nuclear resonance reactions (see another experiment in these series). An example of such a reaction is $^{24}Mg(\alpha,\gamma)^{28}Si$ and its three resonances at energies of 2435, 2866 and 3198 keV [23]. If the initial energy of the ion beam is already sufficiently accurately known this step can be omitted.

The conversion of the pulse height analyser channel number to backscattered ion energy can be carried out by bombarding pure elemental thin film targets (same bombarding energy, same geometry, and several elements should be measured to warrant wide calibrated energy range). Typical calibration samples could be: Ti/Si substrate, Ag/Si substrate, Au/Si substrate and so on.

To get the RBS spectrum of the thin film:

(1) Collect the RBS spectrum of the sample to be analysed.

(2) Record the collected charge used in the sample RBS measurement.

Note: In all measurements adjust the detector count rate to a reasonable level to exclude detection dead-time-corrections.

Sn-Bi thin film sample spectrum:

As a sample case a thin bi-elemental Sn-Bi alloy film grown on a Si substrate is characterised. The RBS spectrum obtained from the sample by 3 MeV alpha particles is shown in Figure 40. The experimental parameters in the measurements were as follows:

(1) detection angle 165° (Cornell geometry);
(2) ion energy 3 MeV He^{+};
(3) collected charge 37 nC;
(4) detection solid angle 43.48 msr;
(5) energy resolution 18 keV;
(6) detector energy calibration E_0 = -85.3 keV and k = 8.188 keV/channel;
(7) area of experimental Si yield 19274 counts;
(8) area of experimental Sb yield 768 counts;
(9) area of experimental Bi yield 812 counts;
(10) area of simulated Si yield 19604 counts;

(11) area of simulated Sb yield 954 counts;
(12) area of simulated Bi yield 1047 counts.

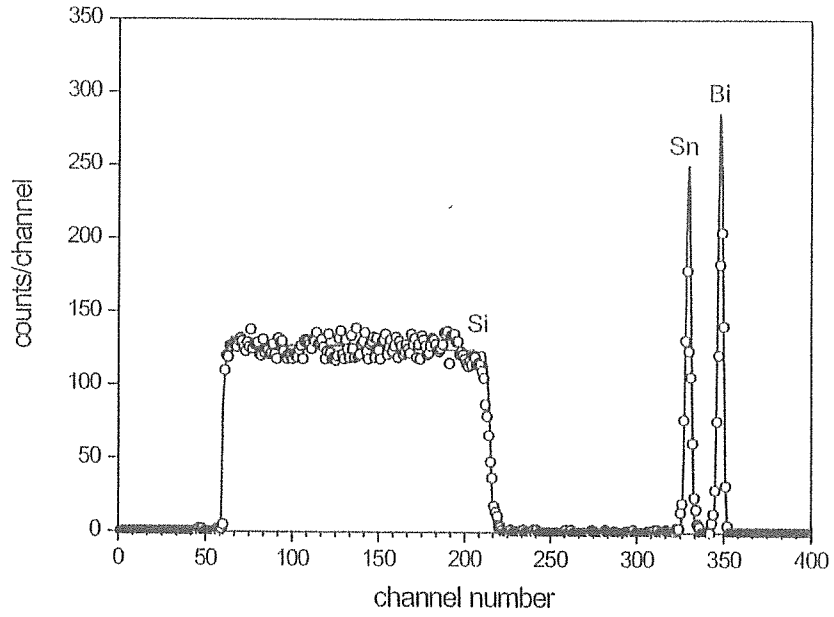

FIG. 40. RBS spectrum obtained of a thin film of Sn_xBi_y alloy grown on Si substrate. For experimental parameters see the text.

4.6.5. Data analysis

Using the guidelines and equations provided in the theoretical part of these instructions:
(1) Identify the sample elements by using Eqs. (75) and (76);
(2) Calculate the average stoichiometry of the film using Eq. (78);
(3) Calculate the sample film areal density by Eq. (77).

The corresponding simulated spectrum obtained by using the computer code RBX [29] is shown by the solid red line. The experimental parameters were used as input to the program. The simulation yields a stoichiometry of $Sn_{0.74}Bi_{0.26}$ and a film areal density of approximately 1.2×10^{17} atoms/cm^2.

Some other commonly utilised RBS computer codes besides RBX are SIMNRA [20], NDF [21] and RUMP [30].

4.6.6. Concluding remarks

The most common RBS computer codes are listed in Ref. [23] along with proper references and the code distribution modes. A comprehensive presentation of the various simulation programs can also be found in Ref. [23]. Finally, it should be noted that by taking advantage of the increased, non-Rutherford, cross-sections at high He ion energies, the sensitivity for the detection of light elements can be improved significantly. The procedures of utilising the enhanced cross-sections in analytical work (including utilisation of the cross-section resonances for light element depth profiling) may be found in Ref. [23] along with appropriate cross-section data.

4.6.7. Recommended equipment

- Scattering chamber (light tight), with current integration;
- Particle detector with standard electronics for spectroscopy;
- A thin film sample deposited on a light substrate (e.g. silicon).

4.6.8. Safety precautions

In case the sample contains significant concentrations of light elements, one should note the possibility for prompt gamma ray and neutron emission. Radiation level should be measured prior to the experiment, and constantly monitored throughout. If necessary, use the appropriate shielding and working distance to minimise any potential exposure risks.

5. ACCELERATOR NUCLEAR INSTRUMENTATION EXPERIMENTS

5.1. MEASUREMENT OF THE EFFICIENCY CURVE OF AN X RAY DETECTOR

Contrary to charged particle detectors where the detection efficiency is 100% and is not dependant on ion energy, the intrinsic detection efficiency for Si(Li) X ray detectors strongly depends on the X ray energy. The non-constant detection efficiency of a Si(Li) detector must be taken into consideration when making elemental analysis using PIXE. For low-energy X rays (1–3 keV), the intrinsic detection efficiency is very low and thus the sensitivity for PIXE measurements of Al, Si, P and Cl using their characteristic K_α X ray lines is low. This experiment will measure the intrinsic detection efficiency in the region 1–10 keV.

5.1.1. Theoretical background

A Si(Li) X ray detector can be geometrically modelled, as shown in Figure 41. The sensitive detection volume is a silicon crystal. A gold contact layer is deposited on the crystal and beneath this is an inactive silicon dead layer. The Si crystal is maintained at liquid nitrogen temperatures in a cryostat which has a thin Be window to allow the X rays to pass through. These four thicknesses are normally provided by the detector manufacturer in the detector's specifications. In addition, the presence of the ice layer at the surface of a Si(Li) detector should be also taken into account. This layer is formed due to condensation of the water molecules onto the Si crystal that is kept at the liquid nitrogen temperature and can be a few tens of μm thick after a few years of operation.

X rays incident on this system are attenuated by the Be window, ice layer, Au contact and Si dead layers. The transmitted X rays are then absorbed by the Si crystal, producing electron-hole pairs which generate an electrical pulse of amplitude proportional to the energy of the X ray.

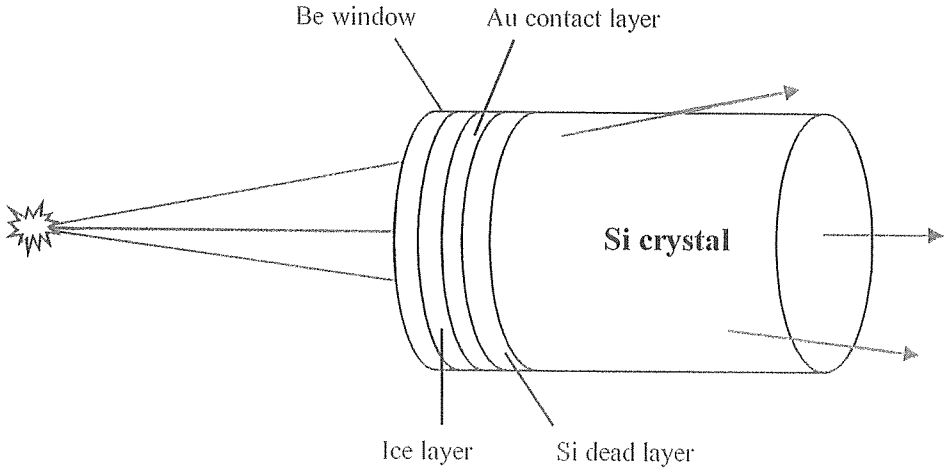

FIG. 41. Schematic model of a Si(Li) X ray detector.

Using this model, the detector efficiency $\varepsilon(E)$ at energy E can be described by Eq. (82):

$$\varepsilon(E) = T(E) \times A(E) \tag{82}$$

Where T(E) is the fraction of X rays transmitted through the Be window, ice layer, gold contact and Si dead layers, and A(E) is the fraction of X rays absorbed by the Si crystal.

$$T(E) = \exp\ [-\mu_{Be}x_{Be} - \mu_{ice}x_{ice} - \mu_{Au}x_{Au} - \mu_{Si}x_{Si}^{d}] \tag{83}$$

$$A(E) = 1 - \exp[-\mu_{Si}^{p}x_{Si}] \tag{84}$$

Where μ_{Be}, μ_{ice}, μ_{Au} and μ_{Si} are the total mass attenuation coefficients for X ray of energy E in the Be window, ice layer, Au contact and Si dead layer and x_{Be}, x_{ice}, x_{Au} and x_{Si}^{d} are the thicknesses of those materials. μ_{Si}^{p} is the photoelectric absorption coefficient at energy E and x_{Si} is the thickness of the active Si crystal. The absorption coefficients can be found in Ref. [31] or obtained from the XCOM program [32]. For our detector x_{Be} = 25 μm, x_{Au} = 10 nm, x_{ice} = 0 nm, x_{Si}^{d} = 0 nm and x_{Si} = 3 mm. The calculated detector efficiency using this data is shown in Figure 42.

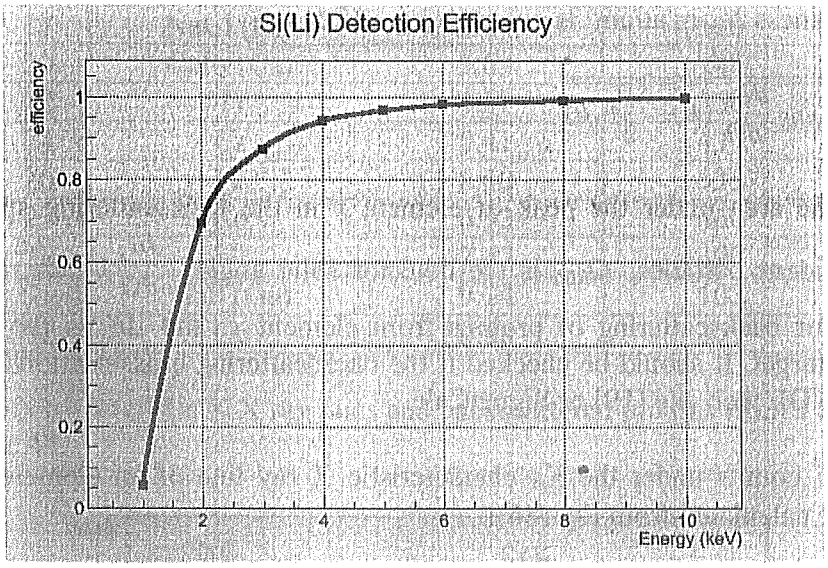

FIG. 42. Calculated intrinsic Si(Li) detector efficiency using XCOM Photo Cross-Sections.

In this low-energy region, $A(E)$ = 1.0 (i.e. transmitted X rays are completely absorbed by the Si crystal). Here, the shape of the efficiency curve is completely determined by the attenuation of X rays through the Be window, ice layer, Au contact layer and Si dead layer.

Following the method proposed by Lennard and Phillips [33], the Si(Li) detector efficiency can be measured by detecting proton induced X rays from a set of thin calibration targets simultaneously with the elastically backscattered projectiles. The spectrum of elastically backscattered projectiles can be used to determine the target thickness. It is assumed that the X ray production cross-sections as well as non-Rutherford backscattering cross-sections are well-known for used elements. As the yield of backscattered particles and X rays are both proportional to the product of the number of incident protons and the target thickness, the ratio of X ray yield to proton backscattered yield is independent of these two quantities. Thus, the detector X ray efficiency can be determined without knowing them, as will now be described.

The experimental geometry is shown at Figure 43.

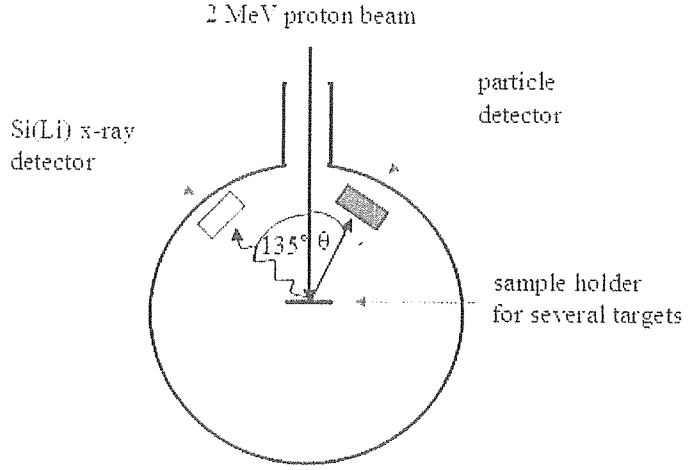

FIG. 43. Experimental setup for Si(Li) detector efficiency determination.

The target thickness N_x, in at/cm^2 is given by Eq. (85):

$$N_x = \frac{A_x}{Q\Omega_{RBS}\frac{d\sigma_x}{d\Omega}(E-\frac{\Delta E_x}{2},\theta)} \tag{85}$$

Where A_x is the area under the peak of element x in the backscattering spectra, Q is the number of incident particles, Ω_{RBS} is the detector solid angle, $\frac{d\sigma_x}{d\Omega}(E-\frac{\Delta E_x}{2},\theta)$ differential cross-section for backscattering of protons from element x, and ΔE_x is the energy loss of protons in the target. It should be checked if the backscattering cross-sections are Rutherford using the IBANDL web site [19] or SigmaCalc.

The number of counts under the K_α characteristic X ray line of an element x is the yield $Y_{xK\alpha}$ and can be calculated from Eq. (86):

$$Y_{xK\alpha} = \frac{\Omega_x}{4\pi} Q N_x \sigma_{IK} \omega_K f_{K\alpha} \varepsilon_x \tag{86}$$

Where Ω_x is the solid angle of X ray detector (in this case 3.3 msr), Q is the number of incident protons, N_x is the target thickness, in at/cm^2, σ_{IK} is the ionisation cross-section for the K^{th} shell of element x, ω_K is fluorescence yield for the K^{th} shell, $f_{K\alpha}$ is relative width of K_α X ray line and ε_x is the intrinsic detection efficiency for X ray line of element x.

It can be seen that the quantities Q and N_x are common in both equations. The intrinsic detection efficiency is calculated from Eq. (87):

$$\varepsilon_x = \frac{4\pi Y_{xK\alpha}}{Q\Omega_x N_x \sigma_{IK} \omega_K f_{K\alpha}} \tag{87}$$

5.1.2. Experimental procedure

The measurements must be carried out in a vacuum chamber. The chamber should be light tight as the charged particle detector is sensitive to light (when bias is applied). All spectra are collected to the same number of incident particles i.e. to the same collected charge ($Q = 0.5$ μC in this case). For this system $\Omega(\theta)$ is 7.6 ± 0.3 msr. The list of targets used in present experiment with calculated thicknesses from the backscattering spectra is given in Table 26.

TABLE 26. TARGETS USED FOR THE MEASUREMENTS WITH THICKNESSES CALCULATED USING RUTHERFORD BACKSCATTERING SPECTROMETRY

Z	element/compound	K_α X ray energy (keV)	thickness (10^{15} at/cm^2)
13	Al	1.49	788
14	SiO (Si)	1.74	664
15	GaP (P)	2.01	427
17	NaCl (Cl)	2.62	500
20	CaF_2 (Ca)	3.69	348
22	Ti	4.51	350
24	Cr	5.41	439
26	Fe	6.40	533
27	Co	6.93	460
28	Ni	7.47	390
31	GaP (Ga)	9.24	103
32	Ge	9.88	379

The spectrum of characteristic K X ray lines and backscattered protons from a thin Cr target is shown in Figure 44.

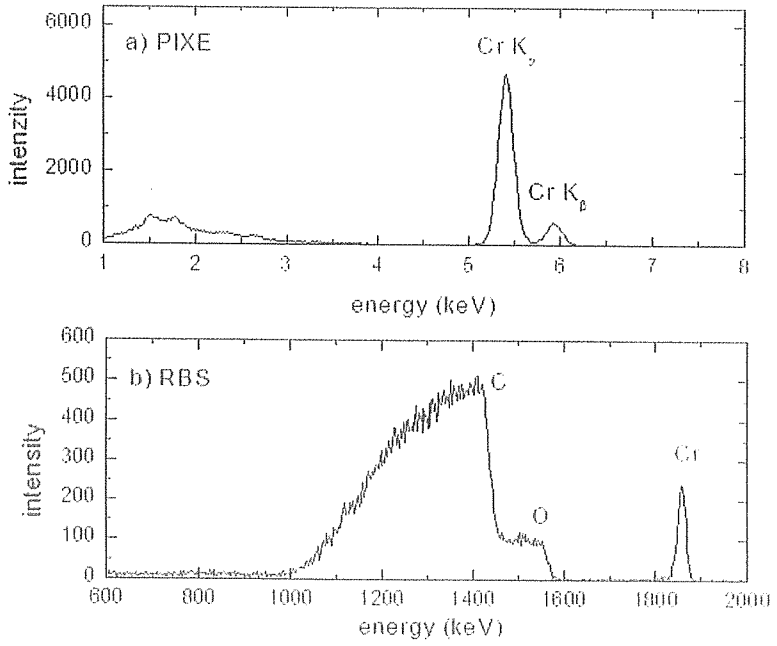

FIG. 44. a) Proton induced X ray spectrum of Cr K X ray lines, b) backscattered protons from the Cr target.

Fluorescence yields ω_K for the K^{th} shell are taken from [34], relative line widths $f_{K\alpha}$ from [35] and the ionisation cross-sections $\sigma_{IK\alpha}$ can be taken from [36]. In this experiment, reference ionisation cross-sections were calculated using the GUPIX subroutine GUCSA. Experimental yields of X ray lines are determined using the spectrum fitting routine in the program AXIL. The GUPIX program as well as any other program that can fit X ray peak shapes can be used as well. All parameters needed for calculation are given in Table 27 together with the calculated detector efficiency using Eq. (87).

TABLE 27. IONIZATION CROSS-SECTIONS FOR K SHELL σ_{IK}, FLUORESCENCE YIELDS ω_K, RELATIVE WIDTHS OF K_α X RAY LINE $F_{K\alpha}$ AND Si(Li) DETECTOR EFFICIENCY ε_X FOR ELEMENTS USED IN PRESENT WORK

Z	$E_{K\alpha}$ (keV)	σ_{IK} (b)	ω_K	$f_{K\alpha}$	ε_X
13	1.487	29401	0.039	0.986	0.33 ± 0.03
14	1.74	19483	0.05	0.976	0.51 ± 0.04
15	2.013	12910	0.064	0.960	0.64 ± 0.05
17	2.622	5923.9	0.099	0.922	0.68 ± 0.05
20	3.691	1916.4	0.169	0.887	0.85 ± 0.05
22	4.509	941.3	0.226	0.884	0.89 ± 0.05
24	5.412	476.2	0.288	0.882	0.99 ± 0.06
26	6.399	247.8	0.355	0.882	0.95 ± 0.06
27	6.925	179.9	0.388	0.881	1.01 ± 0.05
28	7.472	131.7	0.421	0.880	0.99 ± 0.05
31	9.243	52.7	0.517	0.873	1.02 ± 0.05
32	9.876	39.2	0.546	0.868	0.91 ± 0.05

The final result is plotted in Figure 45 with the detector efficiency values (symbols) calculated from experimental X ray spectra as a function of X ray energy, and the theoretical efficiency curve (Eqs. (82)-(84)) calculated using the subroutine GUCSA (full line) in the GUPIX software package. It is seen that the detector efficiency is significantly less than 100% in the low-energy region and is strongly dependent on the detector parameters. The uncertainty of calculated detector efficiency is between 6% for higher and 9% for lower energies due to higher uncertainty in the fluorescence yield at low energies (10–5% for $10 < Z < 20$ and 5–3% for $20 < Z < 30$).

This convenient technique can be successfully used for measurements of the intrinsic X ray detector efficiency if thin single element standards are available. If the Si(Li) detector efficiency is not known, then the above procedure will yield the absolute detection efficiency instead. The relationship between the absolute and intrinsic efficiencies is given by Eq. (88):

$$\varepsilon_{abs} = \frac{\Omega}{4\pi}\,\varepsilon_{int} \qquad (88)$$

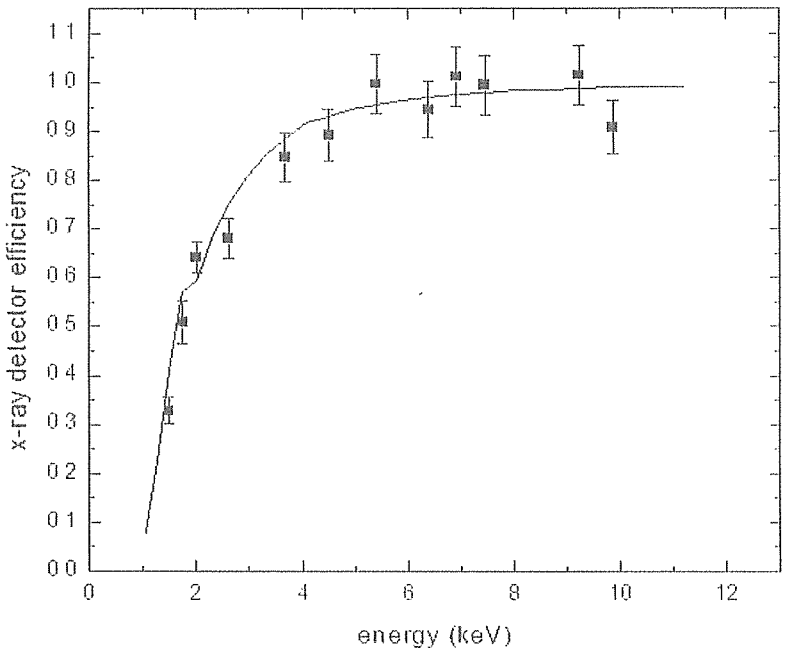

FIG. 45. Si(Li) detector efficiency as a function of the X ray energy (symbols) together with the theoretical efficiency calculated using Eqs. (66)-(68) and GUPIX subroutine GUCSA.

5.1.3. Recommended equipment

- Si(Li) detector;
- Si(Li) detector bias supply;
- spectroscopy amplifier (2 of);
- Charged particle detector;
- Charged particle detector bias supply;
- Analogue to digital converters (2 of) and multichannel analyser to record dual spectra;
- Set of thin calibration foils from $Z = 12$ to $Z = 35$;
- Graphical plotting software;
- X ray spectrum analysis software (e.g. AXIL, GUPIX or GUPIXWIN).

5.1.4. Safety precautions

The proton beam can produce high yields of X rays from collimators and beam-defining apertures if high currents are used and large amounts of the proton beam are incident on these beam trajectory defining components. A radiation survey should be made prior to undertaking measurements and if necessary, use the appropriate shielding and working distance to minimise any potential exposure risks.

5.2. ENERGY AND EFFICIENCY CALIBRATION OF A GAMMA RAY DETECTOR

In order to carry out multi-elemental PIGE analyses, a calibrated (for energy) gamma ray detector is required. For single (and in rare cases for determination of few elements simultaneously) element determinations, a detector with poorer energy resolution than a high purity germanium (HPGe) detector, such as NaI(Tl) or BGO, may be employed. The gamma ray detection system is typically calibrated for energy and efficiency using radioactive point sources for the low-energy gamma rays. In the first part of this experiment HPGe detector is calibrated for energy. This enables practical PIGE measurements of unknown samples for their light element composition. The actual PIGE measurements utilising multi-elemental standard samples for deducing the absolute concentrations are carried out in a separate example. The second part of this experiment deals with determination of the detector efficiency curve.

It should be noted that practical problems may be encountered if very high energy gamma rays are of interest as no common radioisotopes providing such gamma quanta are available. If required, the energy calibration can be easily performed by utilising nuclear reaction induced gamma rays of several light element targets, for example, $^{19}F(p,\alpha\gamma)^{16}O$, $E_\gamma = 6129$ keV. Note that the Doppler broadened gamma ray peaks cannot be used for energy calibration.

5.2.1. Theoretical background

Efficiency is often subdivided into two classes; *absolute and intrinsic*. Intrinsic efficiency does not include the solid angle subtended by the detector as an implicit factor. The two efficiencies are related as:

$$\varepsilon_{int} = \varepsilon_{abs}(4\pi/\Omega) \tag{89}$$

Where Ω is the solid angle of the detector seen from the radiation source position. In this experiment, it is assumed that the detector-source distance is significantly larger than the detector-crystal radius. In this case $\Omega \approx A/d^2$ (A is the detector frontal area and d is the detector-source distance). Determination of intrinsic efficiency is clearly more convenient than absolute efficiency determination. The intrinsic efficiency of a detector usually depends primarily on the detector material, radiation energy, and the physical thickness of the detector in the direction of the incident radiation.

For efficiency calibration one can use any source with known nuclide activity and gamma ray emission probability. Gamma radiation is emitted by excited nuclei in their transition to lower-lying nuclear levels. As an example, the decay scheme of ^{137}Cs is shown in Figure 46. From such decay schemes, the probabilities of various de-excitation transitions (branching ratios) and the number of gamma ray photons per disintegration may be found.

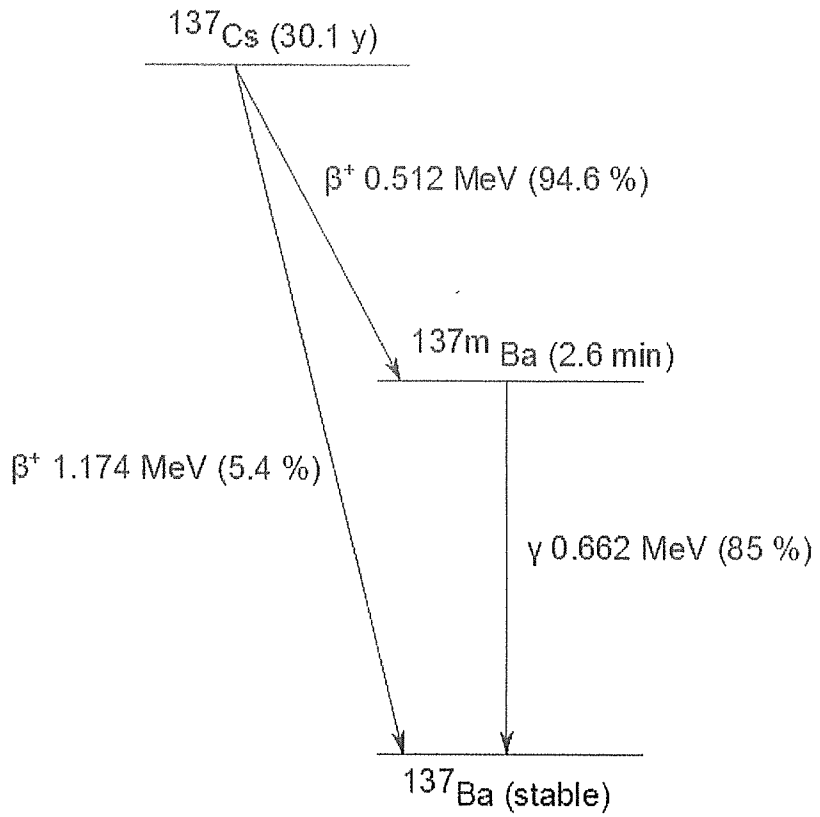

FIG. 46. Decay scheme of ^{137}Cs showing the corresponding branching ratio which should be taken into account in the efficiency determination.

Detector (intrinsic peak) efficiency is the ratio of the detected counts in a full energy peak to the number of the corresponding gamma rays emitted by the source:

$$\varepsilon(E_\gamma) = N_\gamma/N_s = N_\gamma/tpA_o \tag{90}$$

Where N_γ is the number of counts in the photo-peak, N_s is the number of photons emitted from the source. A_o is the activity of the source on the reference date, p is the branching ratio corresponding to energy E_γ and t is the real time of the successive measurements. For simplicity it is also assumed that the source emits radiation isotropically, and that no attenuation takes place between the source and the detector.

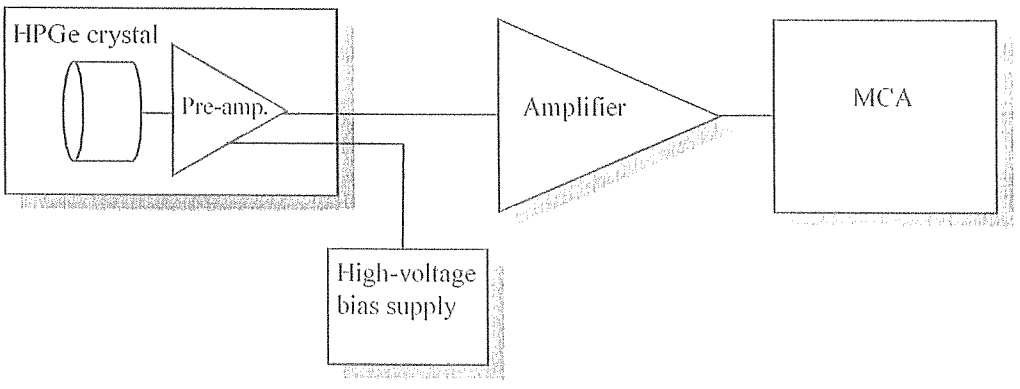

FIG. 47. Gamma ray energy spectrometry system.

5.2.2. Experimental procedure

Prior actual measurements some important points to be considered are:

- check the bias voltage polarity;
- select proper amplifier shaping time;
- adjust the amplifier gain;
- check if pole zero adjustment is necessary;
- check whether unipolar or bipolar pulse shape provides the best energy resolution;
- adjust proper gain for the amplification! Usually an energy region up-to about 6.5 MeV is sufficient (enables determination of fluorine via the reaction $^{19}F(p,\alpha\gamma)^{16}O$), if only low-energy gamma rays are to be detected, the gain can be increased;
- measure gamma ray spectra for all sources and insert the data in Table 28.

The measurement time is not important; it should only be sufficiently long to provide an accurate determination of the peak position.

TABLE 28. PEAK ENERGY VERSUS CHANNEL NUMBER

Source	Gamma ray line energy [keV]	Channel number

Feed the data of Table 28 into the MCA energy calibration program. For details consult the program manuals. Now instead of channel number, the x-axis shows the gamma ray energy.

- Check the source absolute activity at the specified date provided by the source manufacturer (source set specifications sheets);
- Calculate the source activity at the date of the efficiency curve determination;
- Measure each source for good statistics and record the measurement time accurately;
- Determine the peak areas of the gamma ray lines using the peak fitting program;
- Using the calculated source activity, determine the number of gamma rays emitted by the source during the measurement time. Insert the data in Table 29;
- Calculate the solid angle suspended by the detector in order to deduce the absolute efficiency curve;
- Calculate the ratio measured/emitted according to Eq. (90).

TABLE 29. DATA FOR EFFICIENCY CURVE DETERMINATION

γ-energy [keV]	Peak area [counts]	Measurement time [seconds]	Photons emitted by the source	$\varepsilon(E_\gamma)$

In common elemental analysis by the PIGE method, the efficiency of the detector is not required if elemental standard samples are employed. But there are times when efficiency is needed, e.g., when absolute thick target gamma ray yield determinations are of interest. In such cases the detector efficiency multiplied by the solid angle is used as entity and they need not be separated. Now, absorption effects of the low-energy gamma rays are also incorporated intrinsically in the efficiency curve. For such cases, place the sources at the position of the sample in the PIGE set-up.

The branching ratios and relative gamma transition intensities should be taken into account in the calculations (when extracting the number of photons emitted during the measurement) according to the procedure described in the fundamentals part of these instructions. Detector solid angle influence (4π steradians/solid angle of experiment in steradians) should be taken into account when calculating the number of photons emitted by the source.

- Plot the data of Table 29 as energy versus efficiency curve;
- Fit a higher order polynomial ($\varepsilon(E\gamma) = \sum a_i E_i$) to the obtained data.

A typical absolute efficiency curve is shown in Figure 48.

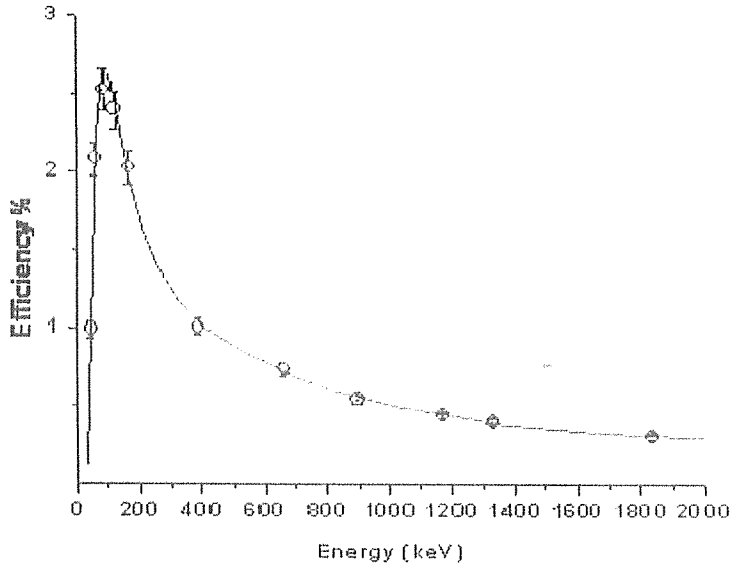

FIG. 48. A typical absolute efficiency curve for HPGe detector.

5.2.3. Concluding remarks

If required, the detection efficiency for the high energy gamma ray energies can be determined by using well-known gamma ray resonance transitions, e.g., the 992 keV resonance of the reaction $^{27}Al(p,\gamma)^{28}Si$ [37].

Despite extremely accurate and careful measurements, the data points in the efficiency curve may scatter somewhat. The curve should be smoothed out for practical use (by the polynomial fit). The data points also include the stated uncertainty of the reference source certified activity.

To improve the accuracy of the absolute efficiency curve, several source-detector distances (solid angles) should be utilised.

If high-activity sources are employed, proper corrections for detector dead time should be conducted when determining the efficiency curve.

The measurement geometry should be arranged so that detection of scattered gamma quanta is prevented.

5.2.4. Recommended equipment

- Detector (with integrated preamplifier);
- Detector bias supply (high voltage);
- Spectroscopy amplifier;
- Analogue to digital converter (ADC) and multichannel analyser (MCA);
- A set of gamma ray reference point sources, e.g. ^{57}Co, ^{137}Cs, ^{60}Co, ^{226}Ra, ^{152}Eu, ^{207}Bi and ^{208}Tl cover the energy range from 0.1 MeV to 3.0 MeV. Also ^{133}Ba, ^{110}Ag sources are commonly employed. The appropriate gamma ray energies and intensity ratios may be found in [23, 38];
- A peak fitting program such as those provided by the MCA vendors (e.g. Gamma Vision by Ortec or Genie-2000 Spectroscopy System by Canberra) is required.

5.2.5. Safety precautions

Even though the required source activities are low and sealed sources are used, the relevant safety regulations must be followed. With knowledge of the source activity and the type of radiation, together with a wise compromise between shielding, distance and exposure time, the risks can be minimised when working with the radioactive sources normally encountered in the laboratory environment.

5.3. ENERGY CALIBRATION OF A SILICON CHARGED-PARTICLE DETECTOR

Charged particle detectors must be calibrated for the detected particle energy in accordance with ion beam methods which are based on particle detection. Such techniques are discussed in the present series of experiments, namely, Rutherford backscattering spectrometry (RBS) and nuclear reaction analysis (NRA) with particle-particle reactions. The detector should be calibrated for the same type of particle as is involved in the actual application.

The most common particle detector used for ion beam analysis has traditionally been Si surface-barrier detectors, where a thin gold layer is used as an electrode. The newer detector type employs ion implantation to form accurately controlled junctions necessary for low reverse leakage currents and thin entrance windows (Passivated Implanted Planar Silicon, (PIPS)). The advantages of these over the surface-barrier detectors (SSB) are discussed in more detail later in these instructions. For light ions (protons and alpha-particles) the detector response is typically quite linear. The overall resolution is typically in the range of 8–15 keV at $E_\alpha = 5.486$ MeV.

5.3.1. Detector choice

When selecting the proper detector type for each experiment, the vendors detector catalogues are of significant help. In the selection one should be careful to pick a detector with a sufficiently thick depletion region to stop the highest expected energy particles, or the energy of these particles will not be measurable. A nomogram shown in Figure 49 may be used to determine the depletion-layer thickness in a Si surface-barrier detector when protons, alpha particles or electrons are to be detected. Note that the depletion layer thickness, silicon resistivity and the required bias voltage are interconnected. As long as the depletion layer is thicker than the particle range, 100% detection efficiency is achieved.

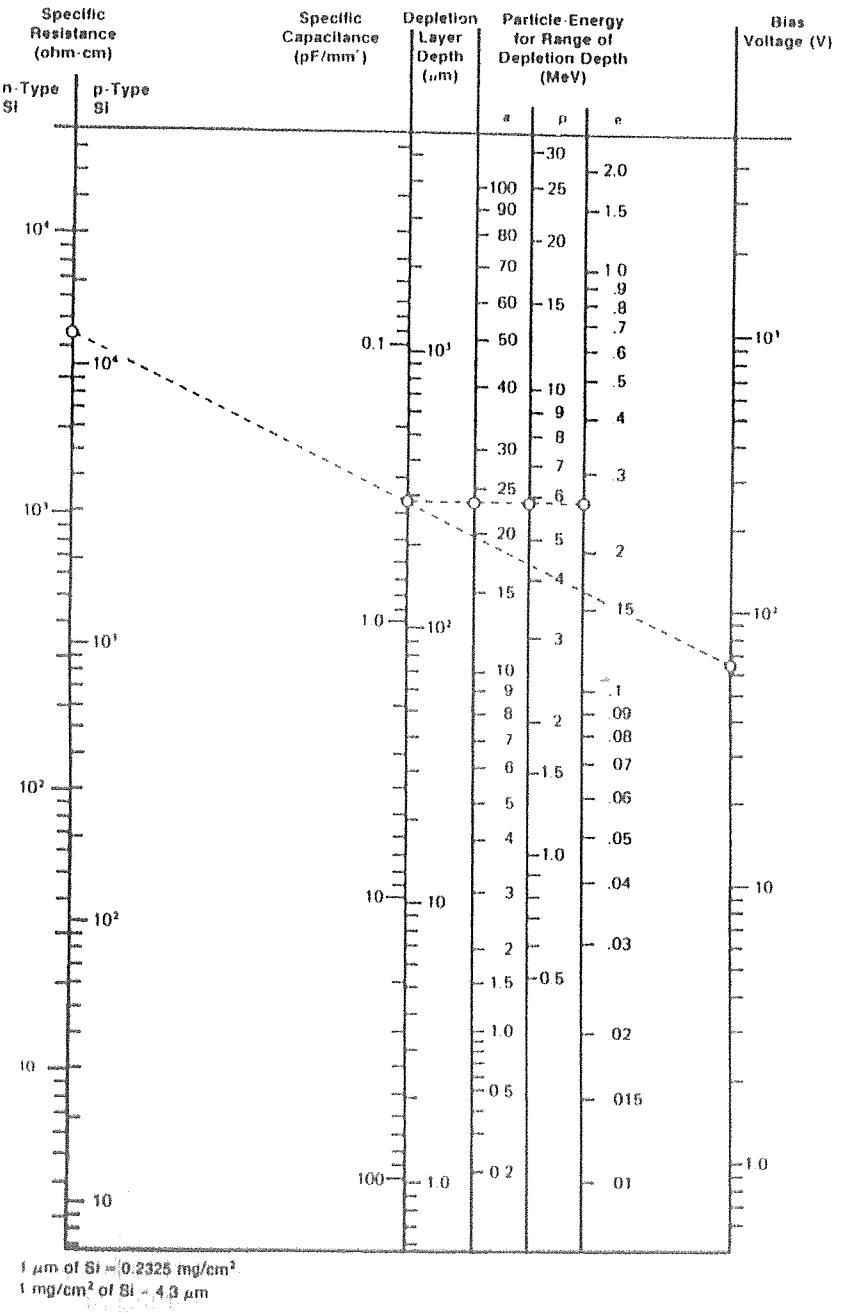

FIG. 49. Silicon surface-barrier detector nomogram showing the relationship between bias, depletion depth and resistivity.

material between the source and the detector and in the detector dead layer should be corrected for. Alternatively, a ^{228}Th source can be employed.

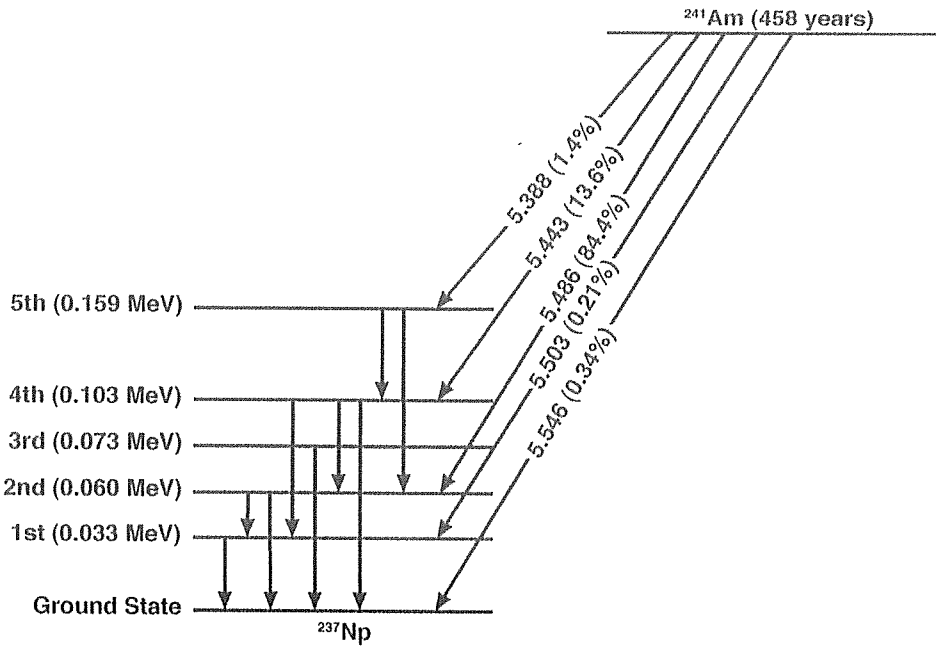

FIG. 51. Decay scheme for ^{241}Am.

The measurements must be carried out in a vacuum chamber. The chamber should be light tight as the detectors are sensitive to light (when bias is applied). A vacuum created by a fore-vacuum pump is sufficient.

5.3.2. Measurements

(1) Carefully place the alpha-source in the vacuum chamber and pump it until a constant pressure reading is achieved.
(2) Increase the detector bias voltage steadily to the specified value. The maximum operating voltage must be kept below the breakdown voltage. The detector specifications provide the maximum voltage rating. Additional protection can be provided by monitoring the leakage current during the experiments.
(3) Measure the energy spectrum for the alpha particles and use the MCA calibration program for channel to energy conversion. Plot the calibration line. A linear response should be noted. Note that an off-set is usually observed at zero.

NOTE: The energy calibration of a particle detector for heavy ions is not as straightforward as it is for light ions (such as alpha-particles in this experiment). This is due to the pulse height defect caused by energy loss due to nuclear collisions which also decreases the detector energy resolution. Energy is lost in the entrance window and the detector dead layer. For dense ionisation, recombination can also occur before the electrons and holes are fully separated.

Eq. (92) becomes:

$$B = K\sqrt{T} \tag{94}$$

The magnet constant K, when determined experimentally, establishes a single-point relationship between the magnetic strength of the analyser magnet and the transmitted proton energy.

For energy calibrations, a comprehensive list of suitable reactions can be found in [23, 39]. The most commonly used reactions are based on:

- neutron threshold measurements such as $^{7}Li(p,n)^{7}Be$ at 1880.4 keV;
- narrow γ resonances such as $^{19}F(p,\alpha\gamma)^{16}O$ at 872.1 keV or $^{27}Al(p,\gamma)^{28}Si$ at 991.9 keV;
- resonances in backscattering such as $^{16}O(\alpha,\alpha')^{16}O$ at 3036 keV.

In this experiment, the γ resonance in $^{27}Al(p,\gamma)^{28}Si$ at 991.9 keV is used for a single-point accelerator energy calibration by measuring the yield of 1778 keV γ ray by HPGe detector This γ ray energy of 1778 keV energy corresponds to the transition from the first excited to the ground state of ^{28}Si, and is emitted at the resonant proton energy of 991.9 keV.

5.4.2. Experimental instructions

The experimental geometry is shown in Figure 52 consisting of:

- A proton beam in the energy range from ~980–1010 keV;
- A scattering chamber with a sample holder for aluminium target;
- A HPGe detector placed at the 45°, 90° or 135° scattering angle and as close as practical to the target;
- Reliable charge collection from a target.

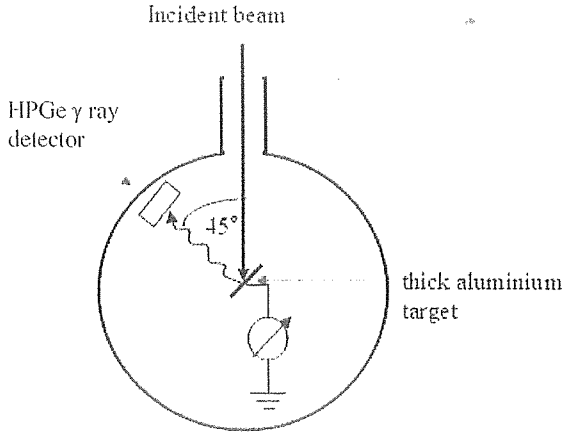

FIG. 52. Experimental setup for accelerator energy calibration using $^{27}Al(p,\gamma)^{28}Si$ reaction and detecting γ rays using HPGe detector.

A thick aluminium target has been used to produce γ rays. In practice it is difficult to use very thin targets because the yield of γ rays, which is proportional to the target thickness, is very small. Therefore it is more common to use a thick target in which the protons are either completely stopped or lose a large percentage of their energy.

The HPGe detector has been placed close to the target and inside the scattering chamber using a recessed access port in the target chamber. The γ ray spectrum for the one of the measurement points (analysing magnet magnetic field $B = 0.27492$ T) is shown in Figure 53. The total collected proton charge for each spectrum was 20 μC, with current during the measurement being ~20 nA.

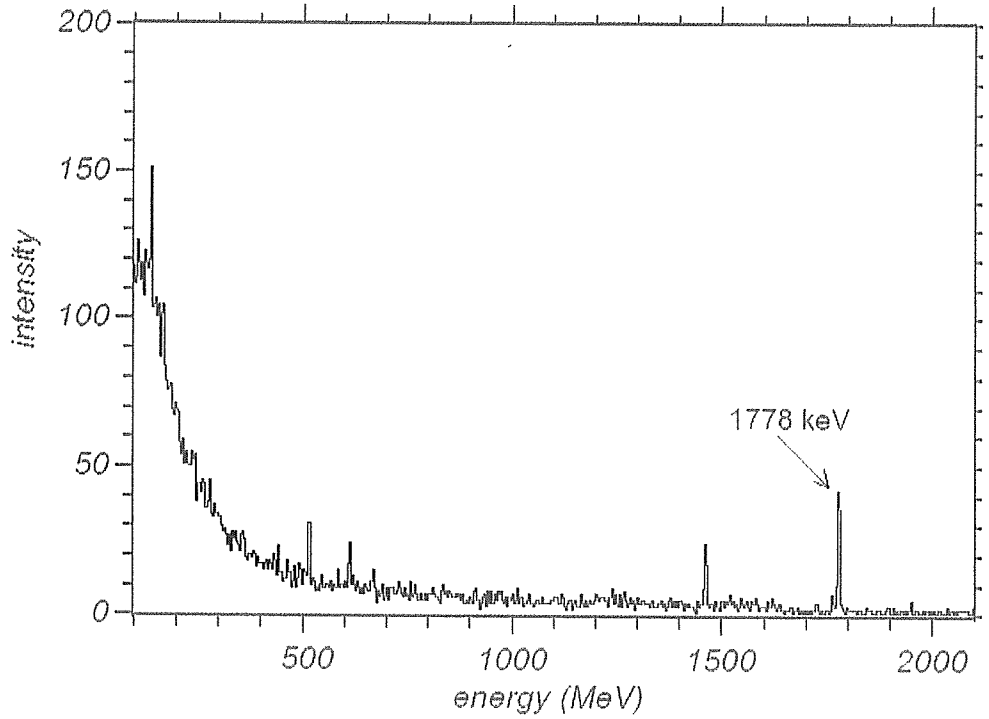

FIG. 53. γ ray spectrum for analysing magnet B=0.27492 T (above the 991.9 keV resonance).

The gamma ray yield, the area (number of counts) under the 1178 keV peak (including the background in this case), is normalised to the total number of protons incident on the target (integrated charge). The excitation function of the $^{27}Al(p,\gamma)^{28}Si$ reaction is determined by repeating the measurements at other accelerator energies near 991.9 keV resonance, and plotting the experimental data as shown in Figure 54.

The half-value height of the plateau corresponds to the resonance peak energy 991.9 keV. A fit of the experimental data with a Boltzmann function using the built-in function in the program ORIGIN 6.0, is shown with red line in Figure 54. The fit yielded a value of $B = 0.27378 \pm 0.00002$ T for the half-height corresponding to the resonance energy $E_0 = 991.9 \pm 0.1$ keV. From Eq. (94), the magnet constant K is calculated to be $K = 0.27490 \pm 0.00003$ T/MeV$^{1/2}$ (n.b. the theoretical fitting function to use is the Error function, if available in the fitting software).

For a more accurate accelerator energy calibration, B versus $\sqrt{T}$ is measured at a number of widely-spaced energies using well-known reactions, and then a linear least-squares fit to the data is made to obtain Eq. (95):

$$B = \overline{K}\sqrt{T} + constant \qquad (95)$$

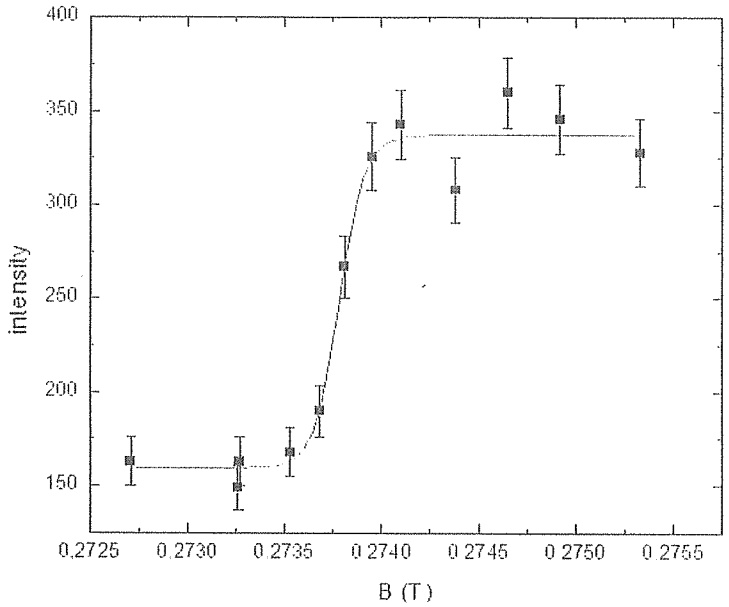

FIG. 54. Thick target γ ray yield for the excitation of $^{27}Al(p,\gamma)^{28}Si$ 991.9 keV resonance as a function of the magnetic field of the analysing magnet.

The front slope of the excitation yield contains information about the energy distribution of the proton beam. By convention, and assuming a Gaussian energy distribution, the energy half-height of the plateau is the energy of the beam (mean of Gaussian), while the region of energies from 10-90% represents the energy width of the beam (Gaussian FWHM).

From the fitted data in Figure 54, the 10% value (B = 0.27367 T) to 90% value (B = 0.273927 T) corresponds to 2 keV at ~1 MeV, or only 0.2 % of the beam energy. This beam width is primarily determined by the accelerator high-voltage instability and finite exit slit opening in the analysing magnet.

5.4.3. Recommended equipment

- Aluminium target;
- HPGe detector;
- Detector bias supply (high voltage);
- Spectroscopy amplifier;
- Analogue to digital converter (ADC) and multichannel analyser (MCA);
- Data fitting and plotting software (e.g. ORIGIN);
- A peak fitting program.

5.4.4. Safety precautions

Certain reactions used for calibration, such as $^{7}Li(p,n)^{7}Be$, produce neutrons in which the yields may be high, depending on the beam current. Additionally, the proton beam can produce high yields of X rays from collimators and beam-defining apertures if high currents are used and large amounts of the proton beam are incident on these beam trajectory defining components. A radiation survey should be made prior to undertaking measurements and if necessary, use the appropriate shielding and working distance to minimise any potential exposure risks.

REFERENCES

[1] INTERNATIONAL ATOMIC ENERGY AGENCY, Research Reactor Database, http://nucleus.iaea.org/RRDB/RR/ReactorSearch.aspx

[2] INTERNATIONAL ATOMIC ENERGY AGENCY, Accelerator Knowledge Portal: http://nucleus.iaea.org/sites/accelerators/Pages/default.aspx

[3] BÖCK, H., VILLA, M., Practical course on Reactor Physics and Reactor Kinetics, Atominstitut/Vienna University of Technology AIAU 26306 (2009).

[4] BÖCK, H., VILLA, M., Practical Course on Reactor Instrumentation. Atominstitut/Vienna University of Technology AIAU 24316, revised (2005).

[5] KHAN, R., KARIMZADEH, S., BÖCK, H., TRIGA fuel burn-up calculations and its confirmation, Nuclear Engineering and Design **240** (2010) 1043–1049.

[6] LAMARSH, J.R., BARATTA, A.J., Introduction to Nuclear Engineering, Prentice Hall, Inc., 3rd edition (2001).

[7] Joint Reactor Laboratory Course, KYOTO UNIVERSITY CRITICAL ASSEMBLY (KUCA), http://www.rri.kyoto-u.ac.jp/CAD/english/training.htm

[8] CANTEACH library, http://canteach.candu.org/

[9] KNOLL, G.F., Radiation Detection and Measurement, John Wiley & Sons Inc., 4th edition (2010).

[10] DUDERSTADT, J.J., HAMILTON, L.J., Nuclear Reactor Analysis, John Wiley & Sons Inc., New York, (1976).

[11] Nuclear Power Fundamentals, Integrated publishing, the most informative site on the internet, http://www.tpub.com/content/doe/h1019v2/css/h1019v2_104.htm

[12] BETHE, H.A., Bremsformel für Elektronen relativistischer Geschwindigkeit, Z. Phys. **76** (1932) 293 (in German).

[13] BLOCH, F., Bremsvermögen von Atomen mit mehreren Elektronen, Z. Phys. **81** (1933) 363 (in German).

[14] Stopping Range of Ions in Matter (SRIM) website, http://www.srim.org/

[15] BOHR, N., DAN, K., The Penetration of Atomic Particles through Matter, Vidensk. Selsk. Mat.-Fys.Medd. **18** (1948) 8.

[16] LIVINGSTON, M.S., BETHE, H.A., Nuclear Physics. C. Nuclear Dynamics, Experimental, Rev. Mod. Phys. **9** (3) (1937) 245.

[17] BERTI, M., et al, $^{12}C(\alpha,\alpha)^{12}C$ Resonant Elastic Scattering at 5.7 MeV as a Tool for Carbon Quantification in Silicon-based Heterostructures, Nucl. Instr. Meth. **B143** (1998) 357.

[18] MIYAGAWA, Y., et al, Oxygen depth profiling in $TiOxSiO_2$ prepared by sol-gel method using $^{16}O(\alpha, \alpha)^{16}O$ resonant backscattering, Nucl. Instr. Meth. **B136-138** (1998) 557.

[19] Ion Beam Analysis Nuclear Data Library (IBANDL) website, https://www-nds.iaea.org/exfor/ibandl.htm

[20] MAYER, M., SIMNRA, User's Guide, Technical Report IPP 9/113, Max-Planck Institut für Plasmaphysik, Garching, Germany (1997), http://home.rzg.mpg.de/~mam/

[21] Ion Beam Analysis DataFurnace website, http://www.surrey.ac.uk/ati/ibc/research/ion_beam_analysis/ndf.htm

[22] Rutherford Universal Manipulation Program (RUMP) website, http://www.genplot.com/RUMP/index.htm
[23] MATERIALS RESEARCH SOCIETY, Handbook of Modern Ion Beam Materials Analysis, 2nd Edition. Editors WANG Y., NASTASI M., Materials Research Society (2009).
[24] BIRD, J.R., WILLIAMS, J.S., Ion Beams for Materials Analysis, Academic Press (1989).
[25] ANTITILA, A., HÄNNINEN, R., RÄISÄŃEN, J., Proton-induced thick-target γ ray yields for the elemental analysis of the Z=3-9, 11-21 elements, J. Radioanal. Chem. **62** (1981) 293.
[26] National Nuclear Data Centre, Brookhaven National Laboratory, http://www.nndc.bnl.gov
[27] Nuclear Data Evaluation Project, Triangle Universities Nuclear Laboratory, http://www.tunl.duke.edu/nucldata
[28] CHU, W.K., MAYER, J.W., NICOLET, M.A., Backscattering Spectrometry, Academic Press, New York (1978).
[29] KÓTAI, E., Computer methods for analysis and simulation of RBS and ERDA spectra, Nucl. Instr. Meth. **B85** (1994) 588.
[30] GENPLOT website, www.genplot.com
[31] THIN, T.P, LEROUX J., New basic empirical expression for computing tables of X ray mass attenuation coefficients, X ray Spectrometry **8** (1979) 85.
[32] BERGER, M.J., HUBBELL, J.H., National Bureau of Standards Report NBSIR. 87-3597 (1987), http://www.nist.gov/physlab/data/xcom/index.cfm
[33] LENNARD, W.N., PHILLIPS, D., Absolute measurement of the photopeak efficiency for a Si(Li) detector: 0.52-8.04 keV, Nucl. Instr. Meth. **166** (1979) 521.
[34] KRAUSE, M.O., Atomic radiative and radiationless yields for K and L shells, J. Phys. Chem. Ref. Data **8** (1979) 307.
[35] SCOFIELD, J.H., Exchange Corrections of K X ray Emission Rates, Phys. Rev. **A9** (1974) 1041.
[36] PAUL, H., MUHR J., Review of experimental cross-sections for K-shell ionization by light ions, Phys. Reports **135** (1986) 47.
[37] ANTTILA, A., KEINONEN, J., HAUTALA, M., FORSBLOM, I., Use of the $^{27}Al(p,g)^{28}Si$, E_p = 992 keV resonance as a gamma ray intensity standard, Nucl. Instr. Meth. **147** (1977) 501.FIRESTONE, R.B., SHIRLEY, V.S., BAGLIN, C.M., CHU, S.Y.F, ZIPKIN, J., Table of Isotopes, John Wiley & Sons, Inc. (1996).
[38] FIRESTONE, R.B., SHIRLEY, V.S., BAGLIN, C.M., CHU, S.Y.F, ZIPKIN, J., Table of Isotopes, John Wiley & Sons, Inc. (1996).
[39] MARION, J.B., Accelerator Calibration Energies, Reviews of Modern Physics **38** (1966) 323.

ABBREVIATIONS

ADC	Analogue to Digital Converter
ALD	Atomic Layer Deposition
CICH	Central Irradiation Channel
CIC	Compensated Ionization Chamber
CSC	Control System Computer
CR	Control Rod
DAC	Data Acquisition Computer
DJ	Diffused junction
ERDA	Elastic Recoil Detection Analysis
FC	Fission Chamber
FE	Fuel Elements
FWHM	Full Width Half Maximum
HIBS	Heavy Ion Backscattering
HPGe	High Purity Germanium
IRMM	Institute for Reference Materials and Measurements
I&C	Instrumentation and Control
MTR	Material Testing Reactor
MCA	Multi-channel Analyser
NIST	National Institute of Standards and Technology
NRA	Nuclear Reaction Analysis
PIXE	Particle Induced X ray Emission
PIPS	Passivated Implanted Planar Silicon
PIGE	Proton Induced Gamma ray Emission
RR	Research Reactor
RBS	Rutherford Backscattering Spectroscopy
SPND	Self-Powered Neutron Detector
SDB	Silicon direct bonding
SSB	Silicon surface barrier
TRIGA	Training, Research, Isotope, General Atomic
UIC	Uncompensated Ionization Chamber

CONTRIBUTORS TO DRAFTING AND REVIEW

Böck, H.	Atominstitut, Vienna University of Technology, Vienna, Austria
Bogdanović Radović, I.	Laboratory for Ion Beam Interactions, Ruđer Bošković Institute Zagreb, Croatia
Khan, R.	Atominstitut, Vienna University of Technology, Vienna, Austria
Li, R.	International Atomic Energy Agency
Mulhauser, F.	International Atomic Energy Agency
Räisänen, J.	Department of Physics, University of Helsinki, Helsinki, Finland
Ridikas, D.	International Atomic Energy Agency
Simon, A.	International Atomic Energy Agency
Villa, M.	Atominstitut, Vienna University of Technology, Vienna, Austria
Vyshniauskas Gomez, J.	International Atomic Energy Agency

IAEA
International Atomic Energy Agency

No. 23

ORDERING LOCALLY

In the following countries, IAEA priced publications may be purchased from the sources listed below or from major local booksellers.

Orders for unpriced publications should be made directly to the IAEA. The contact details are given at the end of this list.

AUSTRALIA
DA Information Services
648 Whitehorse Road, Mitcham, VIC 3132, AUSTRALIA
Telephone: +61 3 9210 7777 • Fax: +61 3 9210 7788
Email: books@dadirect.com.au • Web site: http://www.dadirect.com.au

BELGIUM
Jean de Lannoy
Avenue du Roi 202, 1190 Brussels, BELGIUM
Telephone: +32 2 5384 308 • Fax: +32 2 5380 841
Email: jean.de.lannoy@euronet.be • Web site: http://www.jean-de-lannoy.be

CANADA
Renouf Publishing Co. Ltd.
5369 Canotek Road, Ottawa, ON K1J 9J3, CANADA
Telephone: +1 613 745 2665 • Fax: +1 643 745 7660
Email: order@renoufbooks.com • Web site: http://www.renoufbooks.com

Bernan Associates
4501 Forbes Blvd., Suite 200, Lanham, MD 20706-4391, USA
Telephone: +1 800 865 3457 • Fax: +1 800 865 3450
Email: orders@bernan.com • Web site: http://www.bernan.com

CZECH REPUBLIC
Suweco CZ, spol. S.r.o.
Klecakova 347, 180 21 Prague 9, CZECH REPUBLIC
Telephone: +420 242 459 202 • Fax: +420 242 459 203
Email: nakup@suweco.cz • Web site: http://www.suweco.cz

FINLAND
Akateeminen Kirjakauppa
PO Box 128 (Keskuskatu 1), 00101 Helsinki, FINLAND
Telephone: +358 9 121 41 • Fax: +358 9 121 4450
Email: akatilaus@akateeminen.com • Web site: http://www.akateeminen.com

FRANCE
Form-Edit
5 rue Janssen, PO Box 25, 75921 Paris CEDEX, FRANCE
Telephone: +33 1 42 01 49 49 • Fax: +33 1 42 01 90 90
Email: fabien.boucard@formedit.fr • Web site: http://www.formedit.fr

Lavoisier SAS
14 rue de Provigny, 94236 Cachan CEDEX, FRANCE
Telephone: +33 1 47 40 67 00 • Fax: +33 1 47 40 67 02
Email: livres@lavoisier.fr • Web site: http://www.lavoisier.fr

L'Appel du livre
99 rue de Charonne, 75011 Paris, FRANCE
Telephone: +33 1 43 07 50 80 • Fax: +33 1 43 07 50 80
Email: livres@appeldulivre.fr • Web site: http://www.appeldulivre.fr

GERMANY
Goethe Buchhandlung Teubig GmbH
Schweitzer Fachinformationen
Willstätterstrasse 15, 40549 Düsseldorf, GERMANY
Telephone: +49 (0) 211 49 8740 • Fax: +49 (0) 211 49 87428
Email: s.dehaan@schweitzer-online.de • Web site: http://www.goethebuch.de

HUNGARY
Librotade Ltd., Book Import
PF 126, 1656 Budapest, HUNGARY
Telephone: +36 1 257 7777 • Fax: +36 1 257 7472
Email: books@librotade.hu • Web site: http://www.librotade.hu

INDIA
Allied Publishers
1st Floor, Dubash House, 15, J.N. Heredi Marg, Ballard Estate, Mumbai 400001, INDIA
Telephone: +91 22 2261 7926/27 • Fax: +91 22 2261 7928
Email: alliedpl@vsnl.com • Web site: http://www.alliedpublishers.com

Bookwell
3/79 Nirankari, Delhi 110009, INDIA
Telephone: +91 11 2760 1283/4536
Email: bkwell@nde.vsnl.net.in • Web site: http://www.bookwellindia.com

ITALY
Libreria Scientifica "AEIOU"
Via Vincenzo Maria Coronelli 6, 20146 Milan, ITALY
Telephone: +39 02 48 95 45 52 • Fax: +39 02 48 95 45 48
Email: info@libreriaaeiou.eu • Web site: http://www.libreriaaeiou.eu

JAPAN
Maruzen Co., Ltd.
1-9-18 Kaigan, Minato-ku, Tokyo 105-0022, JAPAN
Telephone: +81 3 6367 6047 • Fax: +81 3 6367 6160
Email: journal@maruzen.co.jp • Web site: http://maruzen.co.jp

NETHERLANDS
Martinus Nijhoff International
Koraalrood 50, Postbus 1853, 2700 CZ Zoetermeer, NETHERLANDS
Telephone: +31 793 684 400 • Fax: +31 793 615 698
Email: info@nijhoff.nl • Web site: http://www.nijhoff.nl

Swets Information Services Ltd.
PO Box 26, 2300 AA Leiden
Dellaertweg 9b, 2316 WZ Leiden, NETHERLANDS
Telephone: +31 88 4679 387 • Fax: +31 88 4679 388
Email: tbeysens@nl.swets.com • Web site: http://www.swets.com

SLOVENIA
Cankarjeva Zalozba dd
Kopitarjeva 2, 1515 Ljubljana, SLOVENIA
Telephone: +386 1 432 31 44 • Fax: +386 1 230 14 35
Email: import.books@cankarjeva-z.si • Web site: http://www.mladinska.com/cankarjeva_zalozba

SPAIN
Diaz de Santos, S.A.
Librerias Bookshop • Departamento de pedidos
Calle Albasanz 2, esquina Hermanos Garcia Noblejas 21, 28037 Madrid, SPAIN
Telephone: +34 917 43 48 90 • Fax: +34 917 43 4023
Email: compras@diazdesantos.es • Web site: http://www.diazdesantos.es

UNITED KINGDOM
The Stationery Office Ltd. (TSO)
PO Box 29, Norwich, Norfolk, NR3 1PD, UNITED KINGDOM
Telephone: +44 870 600 5552
Email (orders): books.orders@tso.co.uk • (enquiries): book.enquiries@tso.co.uk • Web site: http://www.tso.co.uk

UNITED STATES OF AMERICA
Bernan Associates
4501 Forbes Blvd., Suite 200, Lanham, MD 20706-4391, USA
Telephone: +1 800 865 3457 • Fax: +1 800 865 3450
Email: orders@bernan.com • Web site: http://www.bernan.com

Renouf Publishing Co. Ltd.
812 Proctor Avenue, Ogdensburg, NY 13669, USA
Telephone: +1 888 551 7470 • Fax: +1 888 551 7471
Email: orders@renoufbooks.com • Web site: http://www.renoufbooks.com

United Nations
300 East 42nd Street, IN-919J, New York, NY 1001, USA
Telephone: +1 212 963 8302 • Fax: 1 212 963 3489
Email: publications@un.org • Web site: http://www.unp.un.org

Orders for both priced and unpriced publications may be addressed directly to:

IAEA Publishing Section, Marketing and Sales Unit, International Atomic Energy Agency
Vienna International Centre, PO Box 100, 1400 Vienna, Austria
Telephone: +43 1 2600 22529 or 22488 • Fax: +43 1 2600 29302
Email: sales.publications@iaea.org • Web site: http://www.iaea.org/books

14-11791